Journal of Magnetism and Magnetic Materials 483 (2019) 224–248

Contents lists available at ScienceDirect

Journal of Magnetism and Magnetic Materials

journal homepage: www.elsevier.com/locate/jmmm

Research articles

MHD mixed convection and entropy generation in a lid-driven cavity with rotating cylinders filled by a nanofluid using two phase mixture model

Pouya Barnoon[a], Davood Toghraie[b,*], Reza Balali Dehkordi[c], Hossein Abed[b]

[a] Young Researchers and Elite Club, Khomeinishahr Branch, Islamic Azad University, Khomeinishahr, Iran
[b] Department of Mechanical Engineering, Khomeinishahr Branch, Islamic Azad University, Khomeinishahr, Iran
[c] Senior Operations and Executives Engineer of Oil Terminal Company, Kharg Island, Iran

ARTICLE INFO

Keywords:
MHD mixed convection
Entropy generation
Nanofluid
Two phase mixture model

ABSTRACT

In this study, mixed convection and entropy generation in a square cavity containing nanofluid subjected to magnetic field has been studied. A two-phase model (mixture) was used to simulate Newtonian fluid flow and heat transfer in a cavity with rotating cylinders. The Richardson and Hartman numbers ranges are $1 \le Ri \le 100$ and $0 \le Ha \le 30$ respectively. The laminar, two-dimensional (2D), steady and Newtonian flows are assumptions that are considered in this study. The angle of cavity (θ) and dimensionless angular velocity of cylinders (Ω) ranges are $0^\circ \le \theta \le 90^\circ$ and $-3 \le \Omega \le -1$ respectively. The effect of insulation and isothermal ($T = T_c$) cylinders on the flow field and heat transfer has been investigated. The distribution of nanoparticles inside the cavity for different Hartman numbers and Richardson numbers also is investigated. In addition, the effect of the presence of the cylinder on the cavity in stationary and rotating states on the flow field and the increase of the heat transfer rate has been studied. Average and local Nusselt number in terms of Hartman numbers, volume fractions, angles of cavity, isothermal (and adiabatic of cylinders) and angular velocity of cylinders were obtained. The effect of the magnetic field intensity on total entropy generation has been investigated. It's found that by reducing Hartmann number, reducing Richardson number and increasing volume fraction, heat transfer will increase. The presence of the cylinder and its angular velocity also improve the heat transfer. In addition, isothermal cylinders will have a great effect on increasing heat transfer.

1. Introduction

Nanofluids have shown many interesting properties, and the distinctive features offer unprecedented potential for many applications. Magnetohydrodynamics is the study of the magnetic properties and behavior of electrically conducting fluids. Nanofluids are fluids including suspensions of particles of nano size, which had higher thermal characteristics related to the base fluids. Many studies have been done on the properties of nanofluids and their applications in heat transfer systems. However, the first research projects on entropy generation due to nanofluid flow started from 2010.

Rashidi et al. [1] investigated entropy generation in steady MHD nanofluid flow due to a rotating porous disk. The contributions of heat transfer, fluid friction and joule dissipation irreversibility in the averaged entropy generation number for different values of the flow parameters, i.e. magnetic interaction parameter, nanoparticle volume fraction and suction parameter are investigated. Mahmoudi et al. [2] investigated MHD natural convection and entropy generation in a trapezoidal enclosure. They observed that the entropy generation is decreased when the nanoparticles are present, while the magnetic field generally increases the magnitude of the entropy generation. Sheikholeslami et al. [3] investigated MHD effects on nanofluid flow and heat transfer in a semi-annulus enclosure. They found that the enhancement in heat transfer increases as Hartmann number increases but it decreases with increase of Rayleigh number. Chen et al. [4] studied entropy generation in MHD mixed convection nanofluid flow in vertical channel. They found that the local Nusselt number at the cold wall also increases with an increasing nanoparticle concentration. Malvandi et al. [5] studied MHD mixed convection in a vertical annulus filled with nanofluid considering nanoparticle migration. They found that that the advantage of nanofluids in heat transfer enhancement is reduced in the presence of a magnetic field. Fersadoua et al. [6] studied MHD mixed convection and entropy generation of a nanofluid in a vertical porous channel. Their results showed an enhancement on heat transfer rate by using a porous medium, a nanofluid, a magnetic field without taking into account the Joule heating and when mixed convection is assisted.

* Corresponding author at: Department of Mechanical Engineering, Islamic Azad University, Khomeinishahr Branch, Khomeinishahr 84175-119, Iran.
E-mail address: Toghraee@iaukhsh.ac.ir (D. Toghraie).

https://doi.org/10.1016/j.jmmm.2019.03.108
Received 28 November 2018; Received in revised form 12 February 2019; Accepted 25 March 2019
Available online 28 March 2019
0304-8853/ © 2019 Elsevier B.V. All rights reserved.

Mehrez et al. [7] studied MHD effects on heat transfer and entropy generation of nanofluid flow in an open cavity. Their results show that flow behavior, temperature distribution, heat transfer and entropy generation are strongly affected by the presence of a magnetic field. Selimefendigil and Öztop [8] studied influence of inclination angle of magnetic field on mixed convection of nanofluid flow over a backward facing step and entropy generation. They found that the total entropy generation ratio increases with increasing values of Reynolds number, solid volume fraction of nanoparticles and decreasing values of Hartmann number for horizontally oriented magnetic field. Hajialigol et al. [9] studied MHD mixed convection and entropy generation in a 3D microchannel using nanofluid. They found that by enhancing the strength of the imposing magnetic field, heat entropy generation mitigates, while frictional and magnetic ones increase. Sheikholeslami et al. [10] studied MHD free convection of nanofluid considering thermal radiation. They observed that Nusselt number is an increasing function of Rayleigh number, volume fraction of nanoparticle and radiation parameter while it is a decreasing function of viscous dissipation parameter and Hartman number. Selimefendigil and. Öztop [11] studied MHD mixed convection and entropy generation of power law fluids in a cavity. They found that the total entropy generation ratio changes for the Newtonian and dilatant fluids with the magnetic inclination angle and cylinder rotational velocity. Kefayati [12] simulated heat transfer and entropy generation of MHD natural convection of non-Newtonian nanofluid in an enclosure. He found that the increase in the Hartmann number causes the total entropy generation to drop and affects the influences of the power-law index and the volume fraction on the entropy generations. Mamourian et al. [13] optimized mixed convection heat transfer with entropy generation in a wavy surface square lid-driven cavity. They found that increasing of the wavelength of the wavy surface decreases the entropy generation. Hussain et al. [14] numerically investigated MHD mixed convection and entropy generation of nanofluid flow in a double lid driven cavity. A study on nanofluid and multiphase models is presented in various references [31–40]. In addition, further studies on the magnetic field and mixed convection can be found in references [41–51]. Calculation of average Nusselt number, entropy generation, fluid friction and magnetic field, total entropy generation and kinetic energy are the main focus of this study.

In this study, mixed convection and entropy generation in a square cavity containing nanofluid subjected to magnetic field has been studied. A two-phase model (mixture) was used to simulate Newtonian fluid flow and heat transfer in a cavity with rotating cylinders. The Richardson and Hartman numbers ranges are $1 \le Ri \le 100$ and $0 \le Ha \le 30$ respectively. The laminar, two-dimensional (2D), steady and Newtonian flows are assumptions that are considered in this study. The angle of cavity (θ) and dimensionless angular velocity of cylinders (Ω) ranges are $0^\circ \le \theta \le 90^\circ$ and $-3 \le \Omega \le -1$ respectively. The effect of insulation and isothermal ($T = T_c$) cylinders on the flow field and heat transfer has been investigated.

2. Problem statement

The mixed convection heat transfer of a nanofluid inside an H × H square cavity with cylinders subjected to a magnetic field was numerically studied. Inside the cavity, two rotating cylinders were used with identical radiuses (=R), located at equal distances from the walls. The upper and lower walls of cavity were exposed to the hot and cold temperatures of T_H and T_C respectively. The other walls were thermally insulated. The upper wall moves at a constant velocity whereas the lower wall was subjected to a uniform and constant magnetic field The magnetic field in the positive direction of the y-axis enters the wall of the cavity. Both cylinders rotated at a constant angular velocity Ω. Fig. 1 shows a schematic of the problem. The water-Aluminum oxide nanofluid with different volume fractions ($0.01 \le \varphi \le 0.03$) were used. A diameter of 30 nm was assumed for the uniform spherical nanoparticles. The Richardson number (Ri) and the Hartman number (Ha) were assumed to vary in the ranges $1 \le Ri \le 100$ and $10 \le Ha \le 30$, respectively. The horizontal direction of the cavity was assumed to undergo a change in the range $0^\circ < \theta < 90^\circ$. The angular velocity of the cylinders was assumed to vary in the range $-3 < \Omega < 0$. The corresponding effects of thermal isolation of the cylinders as well as isothermal cylinders on the flow field and heat transfer were also studied.

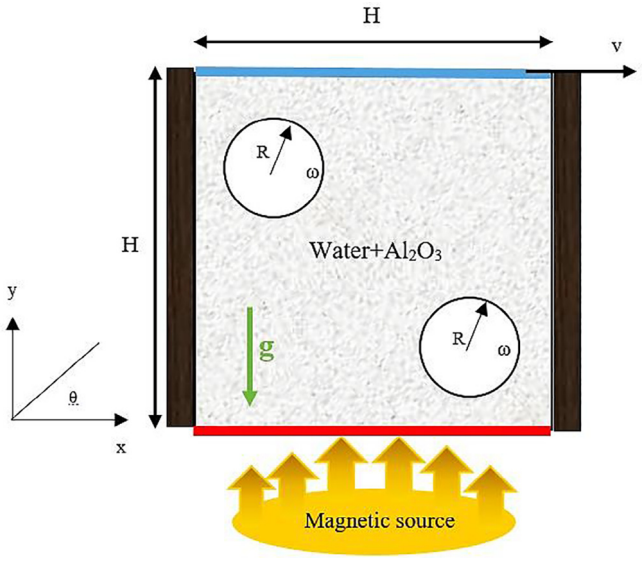

Fig. 1. Schematic of the problem.

3. Mixture model theory

The mixture model is a simplified multiple-phase model which can be used for simulating multiple-phase flows where the phases move at different velocities. This model assumes that the phases are in local equilibrium over short spatial length scales. Through this assumption, the mutual effects of the phases were studied. This model can also use to simulate homogeneous multiple-phase flows with equal phase velocities which exhibit dramatic interphase effects. The other applications of the mixture model include simulating n-phases (two phases in this study) by solving the continuity equation, the momentum equation, and the energy equation for the mixture; the volumetric fraction equation for the secondary phase; and algebraic equations for finding the required relative velocities.

4. Governing equations, heat transfer and flow parameters

The governing equations for the two-dimensional steady flow in the two-phase mixture model are:

Continuity equation:

$$\nabla . (\rho_m \vec{V}_m) = 0 \tag{1}$$

Momentum equation:

$$\nabla . (\rho_m \vec{V}_m \otimes \vec{V}_m) = -\nabla P + \nabla (\mu_m (\nabla \vec{V}_m + \nabla \vec{V}_m^{\,T})) - \rho_m \beta_m (T - T_c) g + \nabla . \left(\sum_{k=1}^{n} \varphi_k \rho_k \vec{V}_{dr,k} \vec{V}_{dr,k} \right) - \sigma_m (\vec{V}_m \times B_0) \times B_0 \tag{2}$$

Once the magnetic field has been applied, the Lorentz force would enter the equation [15]:

$$\vec{F} = \vec{J} \times \vec{B} \tag{3}$$

where $\vec{J}$ is expressed as (Ohm's Law):

$$\vec{J} = \sigma_m(\vec{V}_m \times \vec{B}) \tag{4}$$

where $\vec{B}$ is the vector sum of the applied (B_0) and the induced ($\vec{b}$) magnetic flux densities.

Maxwell's equation is expressed as:

$$\nabla.\ \vec{B} = 0 \tag{5}$$

By combining Ohm's Law with Maxwell's equations, we can obtain the magnetic induction equation as:

$$(\vec{V}_m.\ \nabla)\vec{B} = \frac{1}{\mu_m\sigma_m}\nabla^2\vec{B} + (\vec{B}.\ \nabla)\vec{V}_m \tag{6}$$

Upon solving the magnetic field equation (B), the current density will be calculated in each iteration.

Energy equation:

$$\nabla.\left(\sum_{k=1}^{n}(\rho_k C_{p,k})\varphi_k\vec{V}_k T\right) = \nabla.\ (k_m T) \tag{7}$$

Volumetric fraction equation:

$$\nabla.\ (\varphi_p\rho_p\vec{V}_m) = -\nabla.\ (\varphi_p\rho_p\vec{V}_{dr,p}) \tag{8}$$

where T and P represent temperature and pressure respectively; φ is the volumetric fraction; and V_m is the mass average velocity expressed as [15]:

$$\vec{V}_m = \frac{\sum_{k=1}^{n}\varphi_k\rho_k\vec{V}_k}{\rho_m} \tag{9}$$

In Eq. (2), $V_{dr,k}$ is the drift velocity of the k-th phase, expressed as [15]:

$$\vec{V}_{dr,k} = \vec{V}_k - \vec{V}_m \tag{10}$$

The slip velocity (relative velocity), defined as the ratio of the secondary phase (p) velocity to the primary phase velocity (k), is expressed as [15]:

$$\vec{V}_{pf} = \vec{V}_p - \vec{V}_f \tag{11}$$

The drift velocity corresponding to the relative velocity is expressed as [16]:

$$\vec{V}_{dr,p} = \vec{V}_{pf} - \sum_{k=1}^{n}\frac{\varphi_k\rho_k\vec{V}_{f,k}}{\rho_m} \tag{12}$$

where:

$$V_{pf} = \frac{\rho_p d_p^2}{18\mu_f f_{drag}}\frac{(\rho_p - \rho_m)}{\rho_p}(g - (V_m.\ \nabla)V_m) = V_p - V_f \tag{13}$$

The drag function between the particles is expressed as [17]:

$$f_{drag} = \begin{cases} 1 + 0.15Re_p^{0.687}Re_p \le 1000 \\ 0.0183Re_pRe_p > 1000 \end{cases} \tag{14}$$

Thermophysical properties of the nanofluid including the mixture density (ρ_m), specific heat capacity ($C_{p,m}$), thermal expansion coefficient (β), thermal conductivity (k_m), dynamic viscosity (μ_m), and electrical conductivity (σ_m) are expressed as Eqs. (15)–(20) respectively [18–21]:

$$\rho_m = \rho_f(1-\varphi) + \rho_p\varphi \tag{15}$$

$$(\rho C_p)_m = (\rho C_p)_f(1-\varphi) + (\rho C_p)_p\varphi \tag{16}$$

$$(\rho\beta)_m = (\rho\beta)_f(1-\varphi) + (\rho\beta)_p\varphi \tag{17}$$

$$k_m = k_f\frac{k_p + 2k_f + 2\varphi(k_p - k_f)}{k_p + 2k_f - \varphi(k_p - k_f)} \tag{18}$$

$$\mu_m = \frac{\mu_f}{(1-\varphi)^{2.5}} \tag{19}$$

$$\sigma_m = \sigma_f\left[1 + \frac{3\left(\frac{\sigma_p}{\sigma_f} - 1\right)\varphi}{\left(\frac{\sigma_p}{\sigma_f} + 2\right) - \left(\frac{\sigma_p}{\sigma_f} - 1\right)\varphi}\right] \tag{20}$$

The dimensionless parameters are expressed as [22–24]:

$$Re = \frac{\rho_f vH}{\mu_f} \tag{21}$$

$$Gr = \frac{g\beta_f\Delta TH^3}{\nu_f^2} \tag{22}$$

$$Ri = \frac{Gr}{Re^2} \tag{23}$$

$$Ha = B_0H\sqrt{\frac{\sigma_m}{\rho_m\nu_f}} \tag{24}$$

$$\Omega = \frac{-\omega H}{2v} \tag{25}$$

$$\Theta = \frac{T - T_C}{T_H - T_C} \tag{26}$$

$$S_T = s\frac{T_C^2H^2}{k_m(T_H - T_C)^2} \tag{27}$$

$$X = \frac{x}{H} \tag{28}$$

$$Y = \frac{y}{H} \tag{29}$$

$$U = \frac{u}{v_w} \tag{30}$$

$$V = \frac{v}{v_w} \tag{31}$$

$$P = \frac{p}{\rho_m v_w^2} \tag{32}$$

The local Nusselt number on the hot wall is calculated as [25]:

$$Nu(x) = \frac{h(x)H}{k} \tag{33}$$

$$Nu(y) = \frac{h(y)H}{k} \tag{34}$$

The average convection heat transfer coefficient on the hot wall is expressed as:

$$h(x) = \frac{q''(x)}{T_H - T_c} \tag{35}$$

$$h(y) = \frac{q''(y)}{T_H - T_c} \tag{36}$$

where $q''(x)$ is the heat flux through the hot wall, and T_H and T_c are the temperatures of the hot and cold walls of the cavity respectively.

The total heat flux is obtained by integrating the local heat flux function over the surface of hot wall.

$$q'' = \frac{1}{H}\int_0^H q''(x)dx \tag{37}$$

$$q'' = \frac{1}{H}\int_0^H q''(y)dy \tag{38}$$

Hence, the total convection heat transfer coefficient and the average Nusselt number are calculated as [25]:

$$h = \frac{q''}{\Delta T} \tag{39}$$

$$Nu = \frac{hH}{k} \tag{40}$$

Most heat transfer related processes are exposed to two inevitable losses: thermal losses and friction losses. The entropy generation rate (which includes the irreversibilities due to fluid friction and heat transfer) was obtained by Bejan [26]. In this study, three factors were responsible for entropy generation: viscous effects, heat transfer effects, and magnetic field effects. These are expressed as:(41)

$$s = \frac{k_m}{T_c^2}\left[\left(\frac{\partial T}{\partial x}\right)^2 + \left(\frac{\partial T}{\partial y}\right)^2\right] + \frac{2\mu_m}{T_c}\left[\left(\frac{\partial v_m}{\partial x}\right)^2 + \left(\frac{\partial v_m}{\partial y}\right)^2 + \frac{1}{2}\left(\frac{\partial v_m}{\partial x} + \frac{\partial v_m}{\partial y}\right)^2\right] + \frac{\sigma_m B_0^2}{T_c}(v_m \sin\theta - v_m \cos\theta)^2 \tag{41}$$

In the above equation, the first, second, and third terms represent the entropies generated due to heat transfer effects, fluid friction effects, and magnetic field effects respectively. The dimensionless entropy generation is obtained as follows, in which S_T represents the dimensionless total entropy generation rate per unit volume, which is defined by Eq. (27).

$$S^* = \frac{1}{v}\int S_T dv \tag{42}$$

The dimensionless governing equations are written as follows:

$$\frac{\partial U}{\partial X} + \frac{\partial V}{\partial Y} = 0 \tag{43}$$

$$U\frac{\partial U}{\partial X} + V\frac{\partial U}{\partial Y} = -\frac{\partial P}{\partial X} + \frac{\rho_f}{\rho_m}\frac{1}{Re(1-\varphi)^{2.5}}\left[\frac{\partial^2 U}{\partial X^2} + \frac{\partial^2 U}{\partial Y^2}\right] + \frac{\rho_f}{\rho_m}\frac{\sigma_m}{\sigma_f}\frac{Ha^2}{Re^2}[V\sin\theta\cos\theta - U\sin^2\theta] \tag{44}$$

$$U\frac{\partial V}{\partial X} + V\frac{\partial V}{\partial Y} = -\frac{\partial P}{\partial X} + \frac{\rho_f}{\rho_m}\frac{1}{Re(1-\varphi)^{2.5}}\left[\frac{\partial^2 V}{\partial X^2} + \frac{\partial^2 V}{\partial Y^2}\right] + Ri\frac{\rho_f}{\rho_m}\left(1 - \varphi + \frac{\rho_s}{\rho_f}\frac{\beta_s}{\beta_f}\varphi\right)\Theta + \frac{\rho_f}{\rho_m}\frac{\sigma_m}{\sigma_f}\frac{Ha^2}{Re^2}[U\sin\theta\cos\theta - V\cos^2\theta] \tag{45}$$

$$U\frac{\partial \Theta}{\partial X} + V\frac{\partial \Theta}{\partial Y} = \frac{\alpha_m}{\alpha_f}\frac{1}{RePr}\left[\frac{\partial^2 \Theta}{\partial X^2} + \frac{\partial^2 \Theta}{\partial Y^2}\right] \tag{46}$$

5. Boundary conditions

The dimensional boundary conditions in the present problem are expressed as:

Left wall (Adiabatic): $v_{m,x} = v_{m,y} = 0$, $\frac{\partial T}{\partial x} = 0$

Right wall (Adiabatic): $v_{m,x} = v_{m,y} = 0$, $\frac{\partial T}{\partial x} = 0$

Top wall: $v_m = v_{m,x}$, $T = T_c$

Bottom wall: $v_{m,x} = v_{m,y} = 0$, $T = T_h$

Adiabatic Cylinders: $v_{m,x} = -\omega(y - y_0)$ $v_{m,y} = \omega(x - x_0)$, $\frac{\partial T}{\partial n} = 0$

Isothermal cylinders: $v_{m,x} = -\omega(y - y_0)$ $v_{m,y} = \omega(x - x_0)$, $T = T_c$

6. Thermophysical properties and solution procedure

Table 1 lists the thermophysical properties of the pure fluid and the nanoparticles including density, specific heat capacity, thermal expansion coefficient, thermal conductivity coefficient, and electrical conductivity coefficient.

The finite volume method was deployed to solve the conservation equations. The Boussinesq approximation was used for applying the buoyancy force in the cavity. The pressure based solver was employed for coupling the equations. The second order upwind method was used for interpolating the transfer equation. In this method, values on different planes are obtained via the multi-dimensional linear model. This method has a second order accuracy. The second order upwind method was also used for pressure interpolation. The semi-implicit method for pressure-linked equations (SIMPLE) was used for pressure-velocity coupling. As already mentioned, the finite volume method was used to solve the equations. The following procedure is used in this method:

a) Divide the studied domain into separate control volumes via a computational grid (mesh).
b) Integrate the equations over each control volume to obtain algebraic equations with dependent variables (unknowns) such as velocity, pressure, and temperature.
c) Linearize the independent equations and solve the system of linear equations to obtain new values for the dependent variables.

Table 1
Thermophysical properties of nanoparticles and pure fluid [27,28].

Material	$\rho\left(\frac{kg}{m^3}\right)$	$C_p\left(\frac{j}{kg/K}\right)$	$k\left(\frac{w}{m.k}\right)$	$\beta\left(\frac{1}{K}\right)$	$\sigma\left(\frac{1}{\Omega.m}\right)$
Pure fluid	998.2	4182	0.6	0.00021	0.05
Al_2O_3	3880	733	36	0.85×10^{-5}	10^{-10}

7. Grid independency

Four different grids were used to study the effect of the number of cells on the physical flow and heat transfer parameters. As shown in Table 2, the flow function and Nusselt number were used as the criteria for selecting the final grid. In the absence of a magnetic field, the following values were selected in the grid: Ri = 1, φ = 0.03, and Ω = −1. In view of the obtained percentage error, Grid 3 was selected as the final mesh throughout the simulation.

8. Validation

To check the reliability of the employed numerical solution, the results obtained from the present study were compared with those obtained in other numerical and experimental studies. Figs. 2a and 2b compare the results obtained in the present study with those obtained by Ghasemi et al. [24] who examined the effect of a magnetic field on the convection heat transfer in a cavity filled with a nanofluid. In their study, they used a square cavity filled with the water-aluminum oxide nanofluid for simulation. The right and left walls of the cavity were exposed to cold and hot temperatures respectively while the magnetic field was applied to the left wall. As can be observed in the figures, there is a good agreement between the results obtained in the present study and those obtained in [24].

To further verify the authenticity of the numerical method used, the authors compared their results with the experimental results obtained by Ho et al. [29] as well as the results obtained in [30]. Ho et al. [29]

Table 2
Independence of solution from grid.

Grid	Number of elements	Stream function	Percentage error of stream function	Nusselt number	Percentage error of Nusselt number
G1	8257	1.16770	–	9.50042	–
G2	13,202	1.10935	5.56	10.08963	6.2
G3	**19,297**	**1.08856**	**0.206**	**10.22433**	**1.33**
G4	26,542	1.08736	0.11	10.24717	0.223

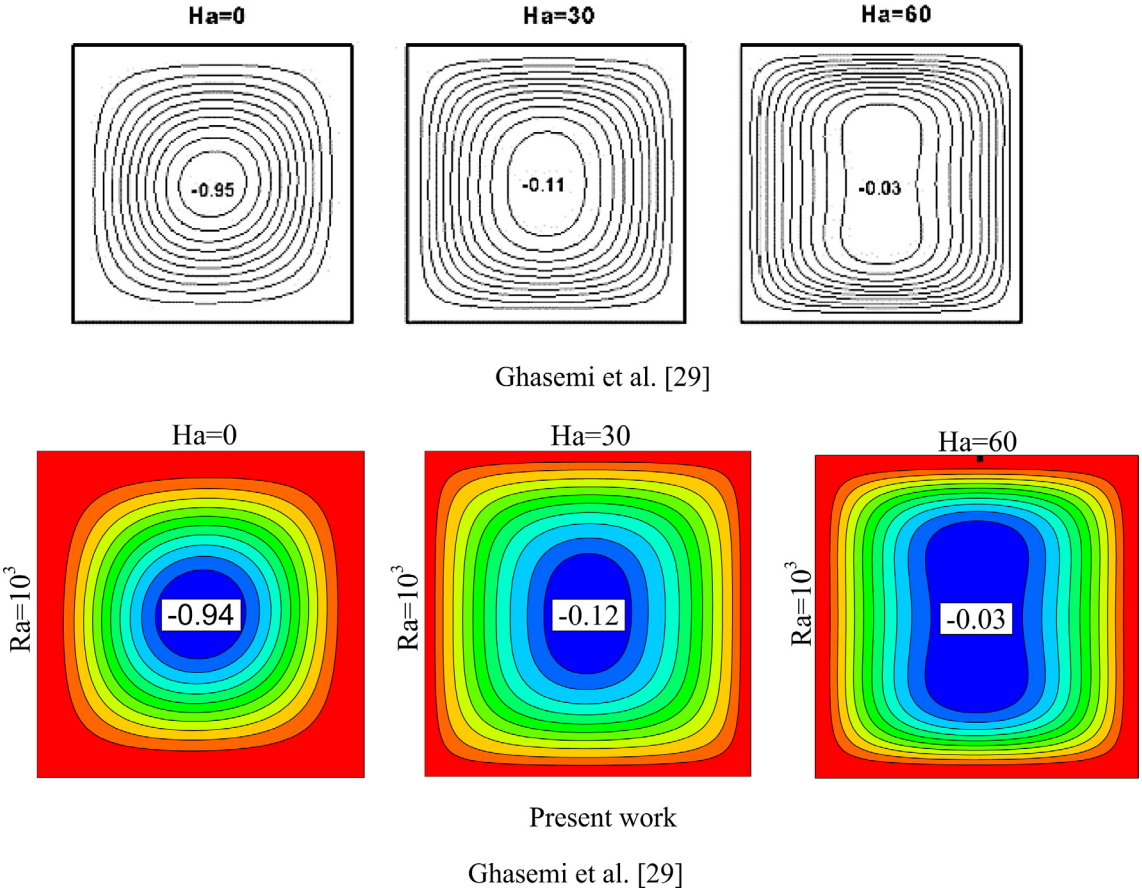

Fig. 2a. Comparison between streamlines contours (present work) with ref. [24].

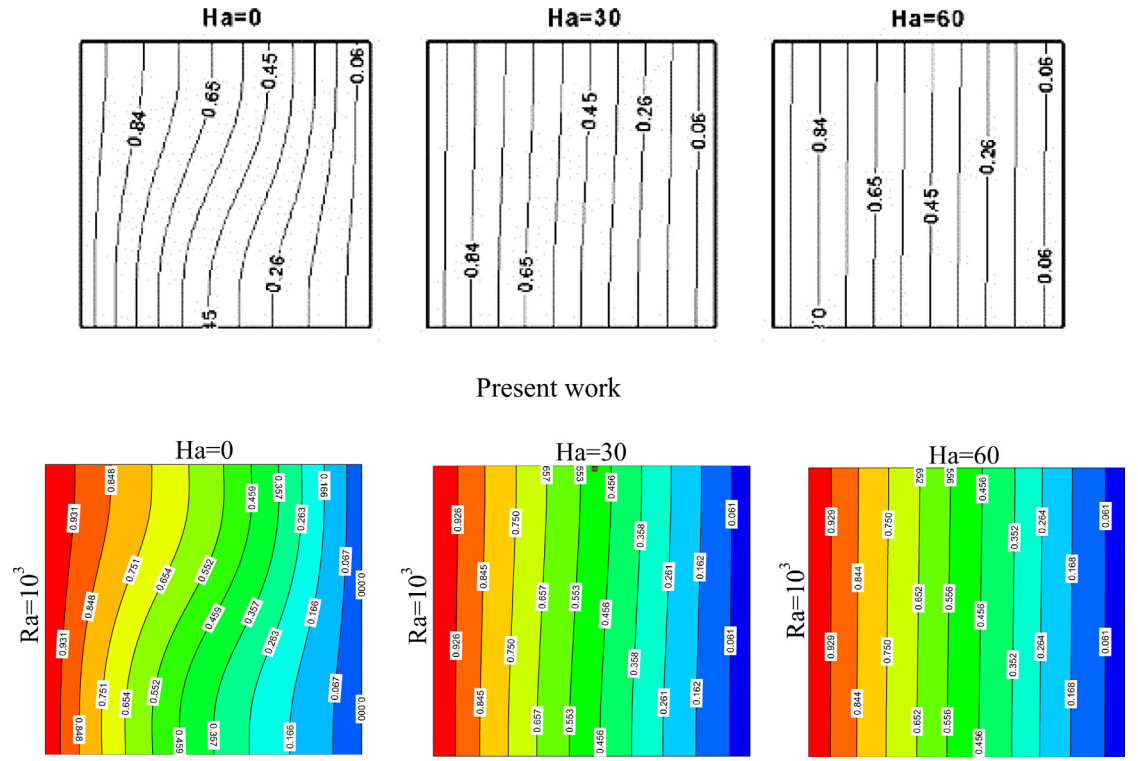

Fig. 2b. Comparison between isotherm lines contours (present work) with ref. [24].

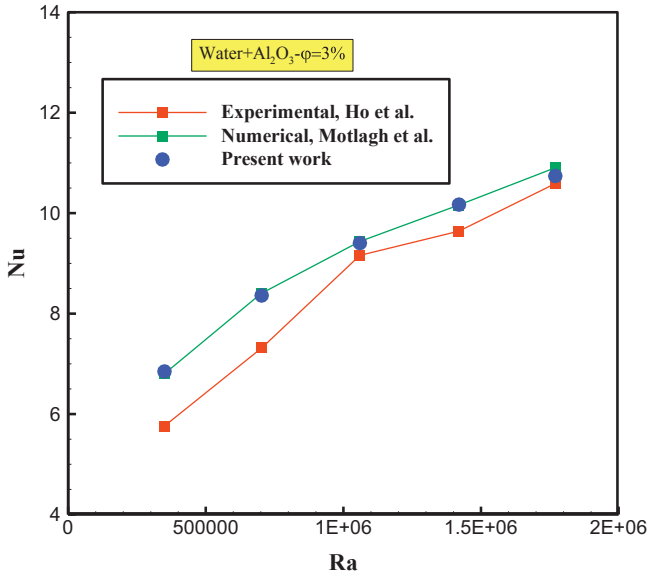

Fig. 3. Comparison between present work with refs. [29,30].

studied the natural convection heat transfer in square cavities filled with nanofluids, using three different cavities with different dimensions. In their experiments, the left and right walls were exposed to hot and cold temperatures respectively while the other walls were thermally isolated. As can be observed in Fig. 3, there is a good agreement between the numerical results obtained in the present study and these experimental results. The slight differences with the experimental results can be attributed to the way the nanofluids were distributed inside the cavity. The results of the present numerical study were also in good agreement with those obtained by Motlagh et al. [30].

9. Results and discussion

9.1. Streamline contours in the absence of a magnetic field

Fig. 4 shows the streamline contours obtained for a pure fluid with a volumetric fraction of 3% at different Richardson numbers and angles. As can be observed, vortices appeared at different locations in the cavity at different Richardson numbers. At the minimum Richardson number, a weak buoyancy force appeared inside the cavity. This gave rise to two main vortices in the vicinity of the cylinders as a result of the rotation of these cylinders. A third vortex was observed in the cavity due to the movement of the upper wall. As the Richardson number was increased, the buoyancy force became more dominant, causing these vortices to grow weaker. Note that, at the greatest (maximum) Richardson number, the position of the vortices changed for different angles. At the maximum Richardson when the cavity made and angle of 0° with the horizontal direction, a major vortex occurred between the cylinders. This vortex gradually grew weaker as the cavity angle was increased to 30°; while a new vortex appeared at the upstream of the two cylinders. Increasing the cavity angle to 60° led to the two vortices being driven towards the left cylinder due to this cylinder being closer to the moving wall of the cavity. Overall, as can be observed, the difference between the fluid and the nanofluid streamlines at greater Richardson numbers was greater due to the difference between the thermal expansion coefficients of the two. At a specific angle, increasing the Richardson number decreased the value of the flow function. In fact, at a constant Grashof number, decreasing the Reynolds number resulted in a corresponding decrease in flow convection within the cavity, ultimately leading to a reduction in the flow function value. However, the same was not true in the case where the cavity made an angle of 60° with the horizontal axis. This can be attributed to the buoyancy force being dominant over the inertial forces at this angle. In addition, at a specific Richardson number, based on the angle the cavity made with the horizontal direction (i.e., the cavity angle), the flow function value can either increase or decrease. As can be observed, the flow function initially increased as a result of the cavity angle increasing to 30° and the Richardson number increasing from 1 to 4; and thereafter exhibited a descending trend. On the other hand, at a Ri = 100, the flow function decreased at cavity angles of less than 30°; however, beyond a cavity angle of 30°, the flow function increased due to, as before, the buoyancy force being the dominant force.

9.2. Isotherm line contours in the absence of a magnetic field

Fig. 5 shows the isotherm line contours obtained for a pure fluid (volumetric fraction = 3%) at different Richardson numbers and different cavity angles. As can be observed, at the minimum Richardson number when forced convection was the dominant flow regime in the cavity, the temperature was almost constant in the center of the cavity between the cylinders. In addition, at lower Richardson numbers, the density of the isothermal lines near the hot wall increased due to higher temperature gradients in this region, with the highest line density occurring at Ri = 1 which gave rise to the greatest heat transfer rate taking place at this Richardson number. At Ri = 4, the line density in the vicinity of the walls did not change since forced convection still governed the flow. At the cavity center, however, the temperature was far from constant. Upon increasing the Richardson number to 100, the temperature at each point in the center of the cavity underwent significant variations as forced convection decreased in this region. In addition, line density in the vicinity of the walls decreased. However, in this case, these two problems could change depending on the angle between the cavity and the horizontal direction. In addition, increasing the Richardson number would increase the thermal boundary layer in the vicinity of the horizontal wall, as a result of which more heat could penetrate into the cavity, which would ultimately reduce the heat transfer rate. At Ri = 1 and Ri = 4, increasing the angle between the cavity and the horizontal direction resulted in more heat entering the cavity center from the left side of the cavity, which would ultimately reduce the heat transfer rate. At Ri = 100, only the cavity angle could influence the isothermal lines pattern due to the increasing dependency of the dominant buoyancy force on this angle.

9.3. Streamline contours in the presence of a magnetic field

Fig. 6 shows the streamline contours obtained for a pure fluid and nanofluid at different Richardson and Hartman numbers and a cavity angle of 60°. As can be observed, at a specific Ri, increasing the Hartman number would reduce the flow function value. In fact, increasing the Lorentz force would weaken the convective flows ultimately reducing the flow function value. As already mentioned, at Ri = 1 and Ri = 4, three vortices (resulting from rotation of the cylinders and movement of the wall) were observed in the absence of a magnetic field. Since the Lorentz force acts perpendicularly to the magnetic field, increasing the Hartman number would cause the vortex in the vicinity of the cylinder to be driven towards the left cylinder, and the streamlines to be driven downwards towards the right thermally isolated wall. Although both cylinders rotated at the same angular velocity, the vortex formed at the back of the right cylinder persisted even after a magnetic field was applied. This is due to the position of the cylinder within the cavity. On the other hand, at Ri = 1 and Ri = 4, the presence of a magnetic field would lead to the formation of a small vortex at the upper part of the left cylinder. This effect is due to the direction of the Lorentz force in the cavity and the ultimate rotation of the left cylinder. In addition, at Ri = 4, increasing the magnetic field strength would lead to smoother streamlines at the cavity center between the cylinders. At Ri = 100, the flow function value for all Hartman numbers was greater than that obtained for Ri = 4. Although,

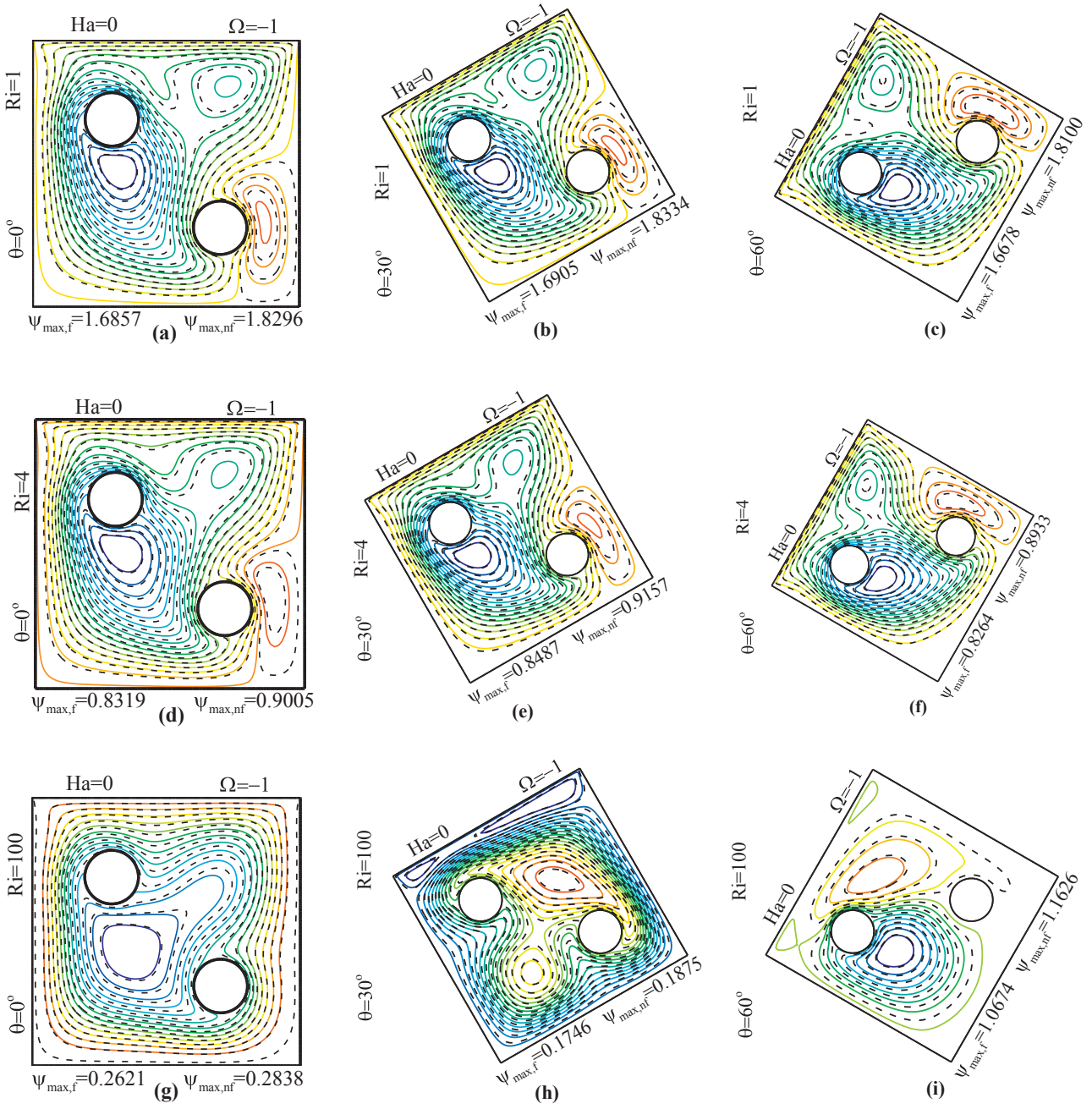

Fig. 4. Streamline contours obtained for different Richardson numbers and cavity angles in the absence of a magnetic field.

in this case, the buoyancy force dominated the convection flow, the flow function value was greater than that obtained for Ri = 4 due to the effect of the cavity angle. In addition, at Ri = 100 in the absence of a magnetic field, a relatively large vortex was formed between the cylinders in the vicinity of the left cylinder. The effect of the magnetic field was more pronounced as the free convection dominated the forced convection, resulting in a more significant contrast between the buoyancy and the Lorentz forces. Increasing the Hartman number resulted in the streamlines being driven towards the right wall. Hence, at Ha = 10, the streamlines were driven towards the right cylinder, thus strengthening the flow around the cylinder, with the ultimate formation of a vortex at Ha = 20 which was further intensified at Ha = 30.

9.4. Isotherm line contours in the presence of a magnetic field

Fig. 7 shows the isotherm line contours obtained for a pure fluid and nanofluid at a cavity angle of 60° and different Hartman and Richardson numbers. As can be observed, at constant Ri, increasing Ha would cause the isothermal lines to be driven into the cavity. These lines were extended towards the cavity center. This reduced the temperature gradient on the hot surface. Therefore, it can be concluded that, at constant Ri, increasing Ha would reduce the rate of heat transfer. In addition, the magnetic field effects on the isothermal line contours were more pronounced as the forced convection was reduced, with the above variations being much more significant at Ri = 4 as compared with Ri = 1. In addition, as penetration of the pure fluid streamlines into the cavity was more than that of the nanofluid, therefore, it was concluded that heat transfer rate in the latter was far greater than that in the former. In the absence of a magnetic field, the isothermal line patterns of the nanofluid were similar to those of the pure fluid. Upon applying the magnetic field, however, differences were observed at the cavity center as well as in the vicinity of the left cylinder between the isothermal

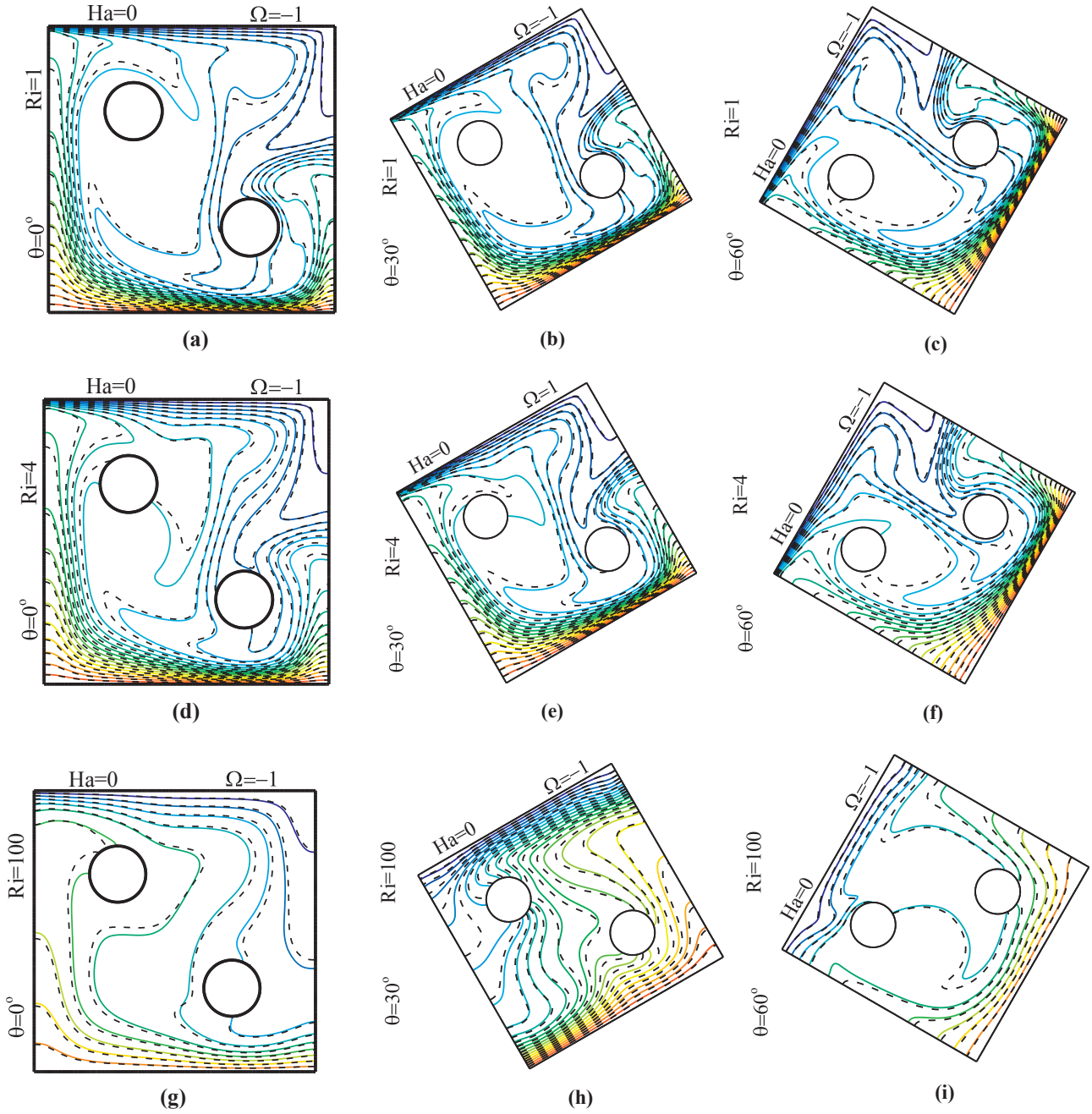

Fig. 5. Isotherm line contours obtained for different Richardson numbers and cavity angles in the absence of a magnetic field.

streamline patterns of the nanofluid and the pure fluid. The reason for this was attributed to the difference between the electric conduction coefficients of the two. Increasing Ri reduced the kinetic energy of the system, leading to the dominance of free convection. Increasing Ha at Ri = 100 further reduced the kinetic energy of the system while giving rise to a conduction heat transfer regime. This in turn led to a reduction in the surface gradients and, ultimately, reduced the rate of heat transfer. Thus, increasing the magnetic field strength resulted in the emergence of isothermal streamlines in the form of layers that were almost parallel to the hot surfaces. In the vicinity of the cylinders, however, this behavior changed due to rotation of the cylinders.

9.5. Nanoparticle distribution contours in the presence of a magnetic field

Fig. 8 shows the nanoparticles distribution contours obtained for a volumetric fraction of 3% and a cavity angle of 60° at different Richardson and Hartman numbers. In the absence of a magnetic field, a nonuniform nanoparticles distribution was observed at lower Richardson numbers. This was due to the fact that the dominance of forced convection in the system caused maximum flow circulation inside the cavity. In addition to movement of the upper plate, rotation of the two cylinders was also a contributing factor in the nanoparticles distribution; as was observed at Ri = 1 and Ri = 4 where the right cylinder played a significant role in the formation of the most nonuniform nanoparticle distribution due to its position, causing the most intensive nanoparticle migration towards the hot wall of the cavity. A uniform nanoparticle distribution was observed at the cavity center between the cylinders. At Ri = 4, a more uniform distribution was observed in the vicinity of the hot cavity wall due to the decrease in forced convection. An almost uniform nanoparticle distribution was observed at the cylinder once the forced convection had been overcome by the buoyancy force. Under such conditions, a slight non-uniformity

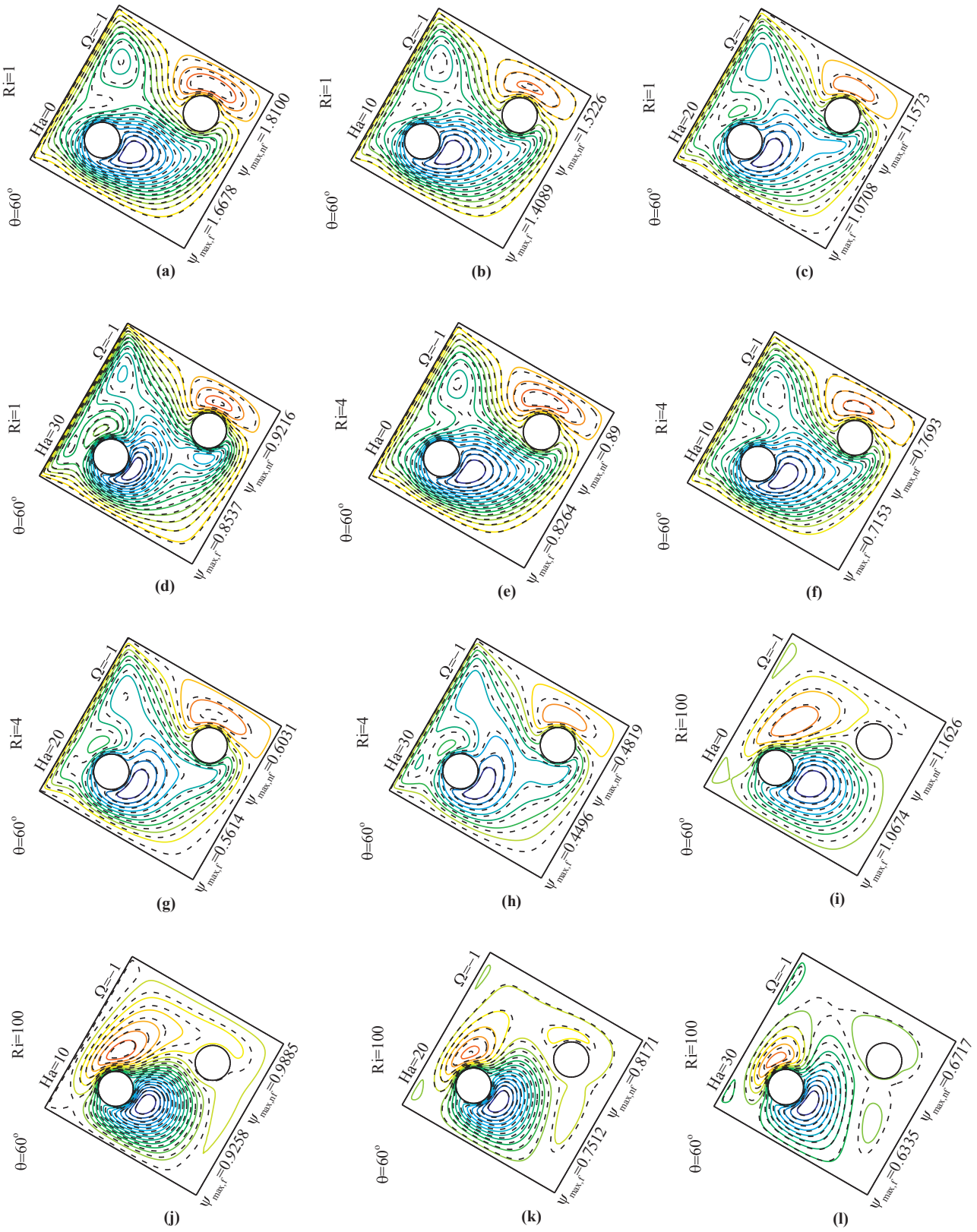

Fig. 6. Streamline contours obtained at a cavity angle of 60° for different Hartman and Richardson numbers.

(unevenness) occurred in the vicinity of the right cylinder due to rotation of the cylinder as well as movement of the upper plate. Nanoparticle distribution in the vicinity of the right cylinder was uniform due to the existing distance between this cylinder and the moving wall. Increasing Ha at constant Ri led to a nonuniform nanoparticle distribution. At lower Richardson numbers, which grew more pronounced as Ri was reduced. As already mentioned, the Lorentz force (which acts perpendicular to the magnetic field) caused the nanoparticles to migrate towards the lower plate, thus driving them towards the cylinder and the thermally isolated wall on the right of the cavity.

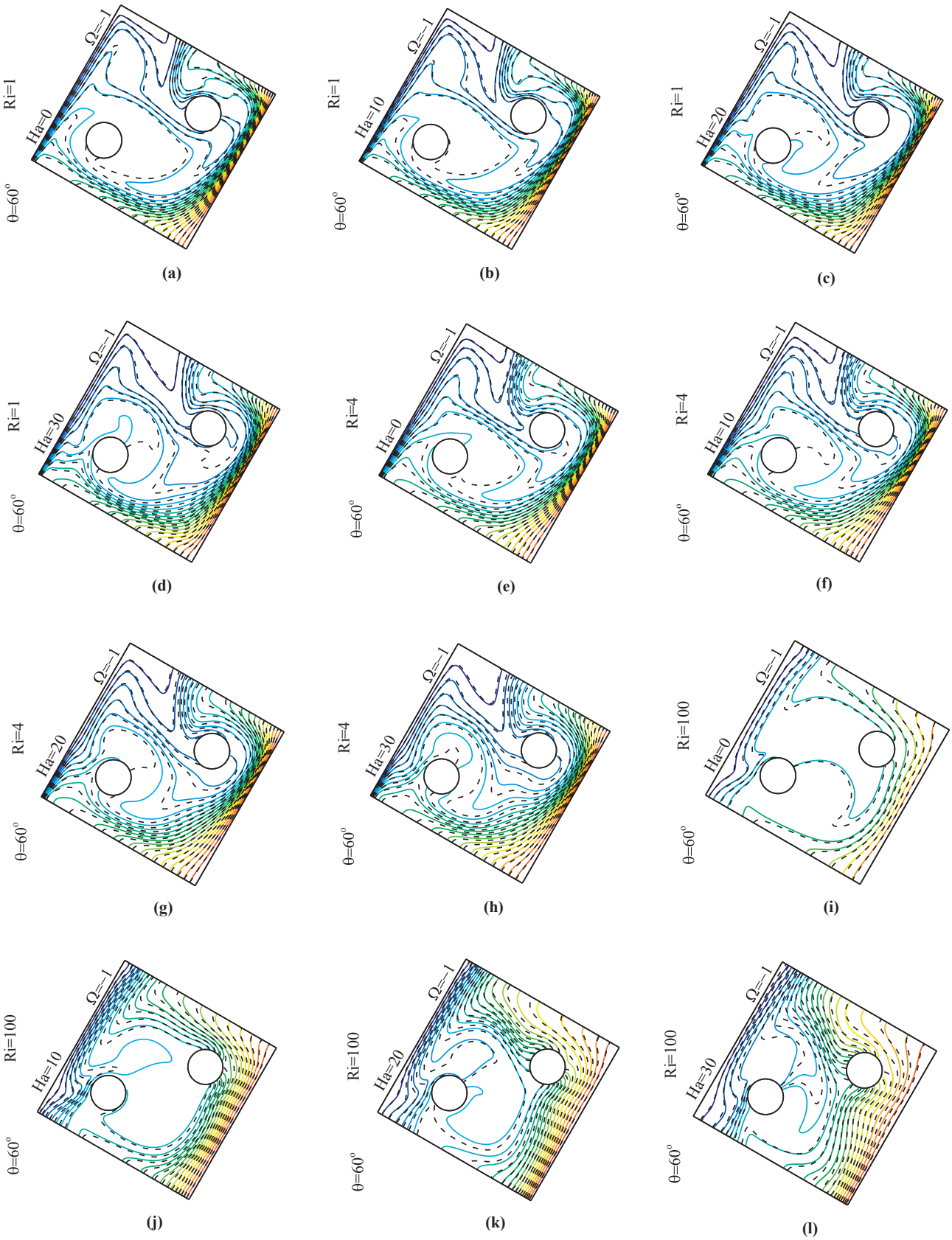

Fig. 7. Isotherm contours obtained at a cavity angle of 60° for different Richardson and Hartman numbers.

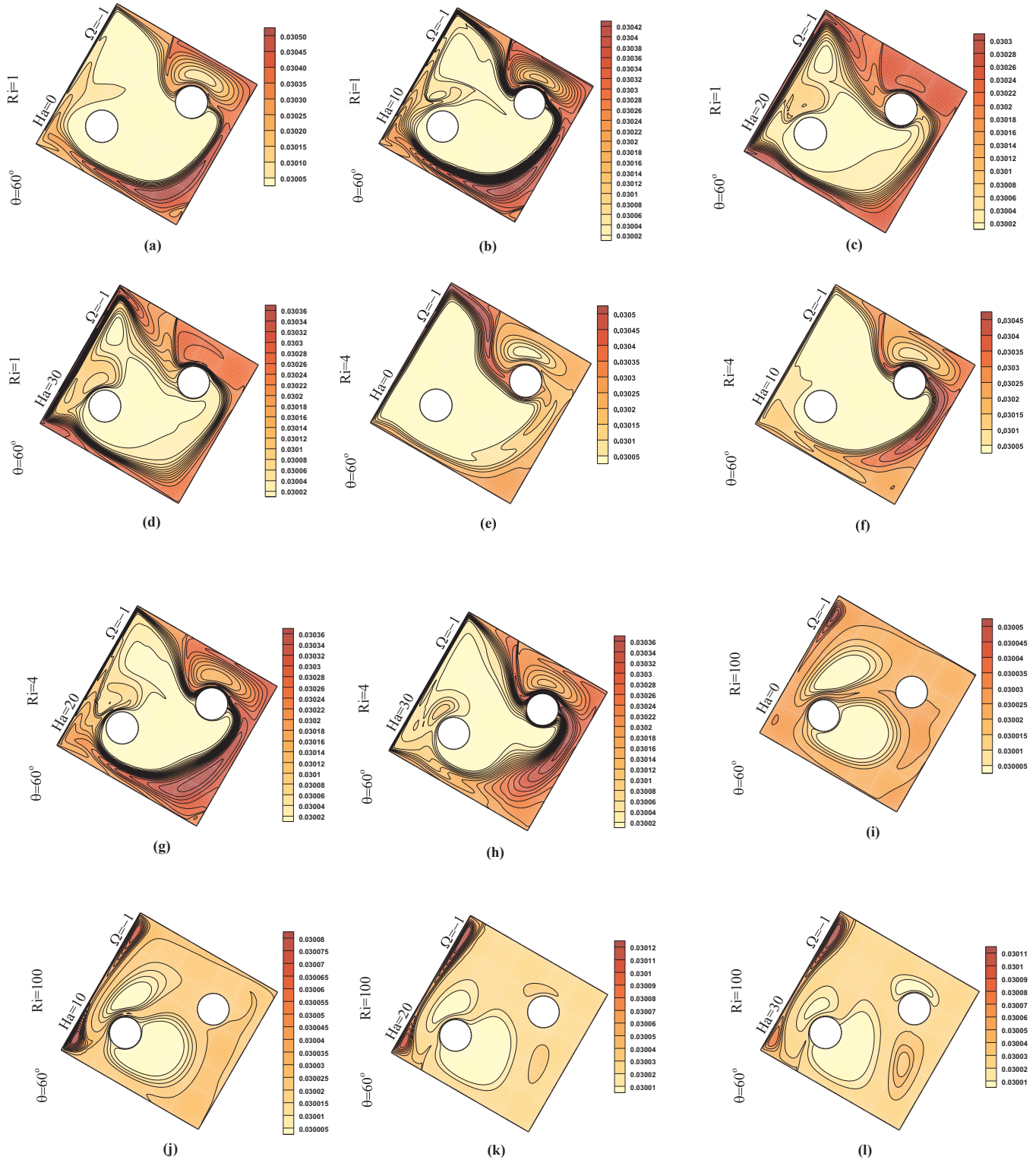

Fig. 8. Nanoparticle distribution contours obtained for a cavity angle of 60° at different Richardson and Hartman numbers.

This was observed at Ri = 1 where nanoparticle migration as well as movement of the moving plate on the one hand, and the Lorentz force on the other gave rise to vortices at the upstream of the right cylinder. As a result of this, the nanoparticles at the upstream of the cylinder were diverted at greater Hartman numbers and were therefore less influenced by the rotating cylinder. Similar results were obtained were obtained at Ri = 4. However, in this case, flow non-uniformity increased at the lower half of the cavity due to the decline in the convection flow as well as the increase Ha, thus causing increasing nanoparticle deposition on the hot wall. Extreme reduction of the convection flow led to a different behavior on the part of the nanoparticles. Thus, at Ri = 100, greater nanoparticle uniformity was observed at both upstream and downstream of the left cylinder as the Lorentz force was increased. In the vicinity of the right cylinder, however, less nanoparticle uniformity was observed due to the Lorentz force acting in the opposite direction to that of the convection flow.

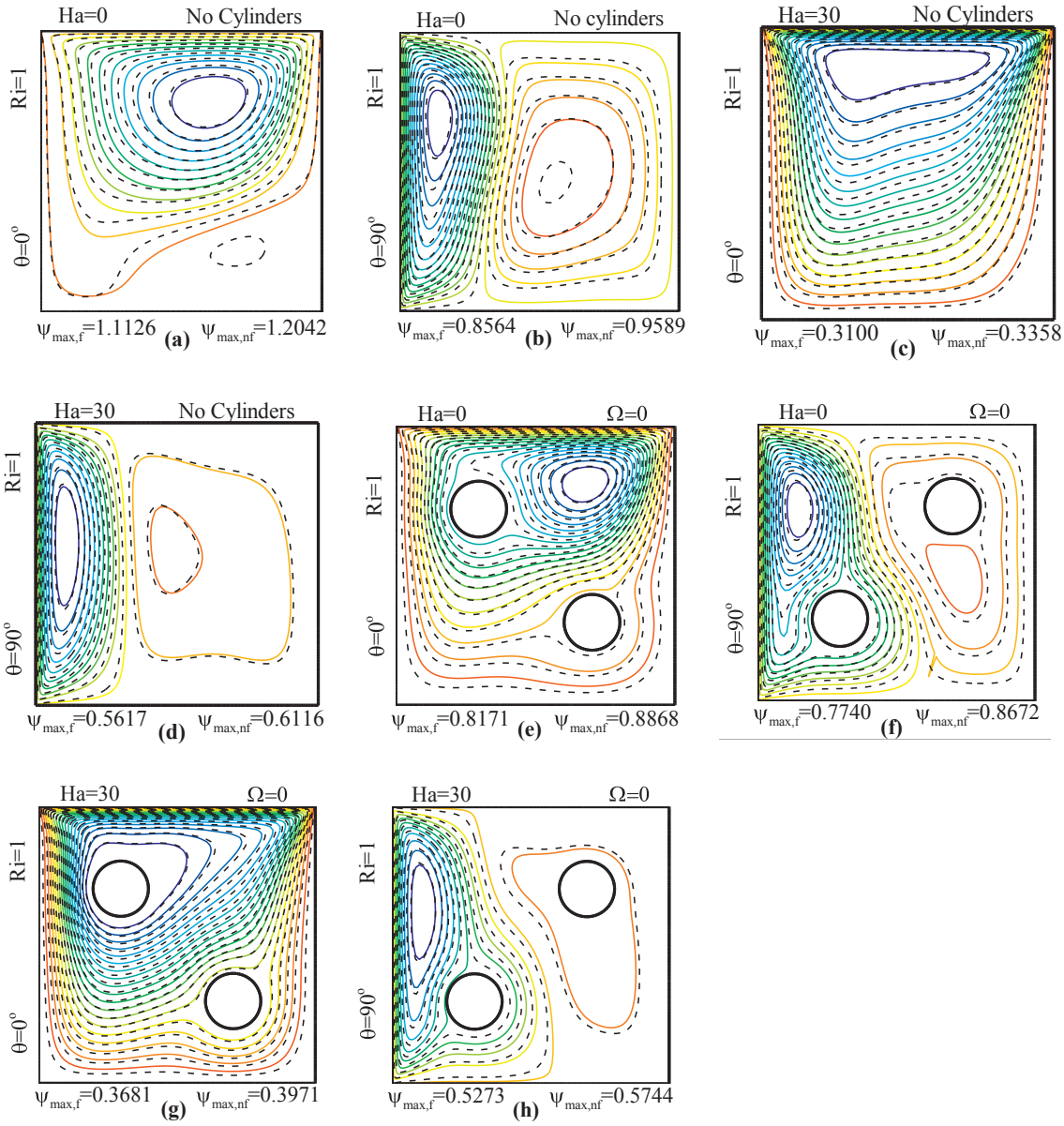

Fig. 9. Streamline contours in the presence and absence of cylinder, obtained for two different angles at minimum and maximum Ha.

9.6. Streamline contours in the presence and absence of cavity cylinders

Fig. 9 shows the streamline contours obtained at two different angles in the presence and absence of a magnetic field. In the case where there was no cylinder in the cavity, the flow function was maximized in the absence of a magnetic field which resulted in better and faster fluid circulation in the cavity, ultimately leading to maximization of the flow function. The greatest flow function variations were obtained at an angle of 0° both in the presence and absence of a magnetic field. In fact, at this angle, the combined effects of the magnetic field and the hot source on the wall maximized the flow function variations. In addition, in the absence of a magnetic field, a major vortex emerged at zero degrees due to the moving upper wall of the cavity. Exposing the cavity to a magnetic field caused the fluid flow to be diverted towards the hot wall, thus forming smoother streamlines. At a cavity angle of 90°, vortices appeared due to the motion of the cavity wall as well as the orientation of the cavity itself. This also led to smoother streamlines; however, due to the reasons mentioned above, the magnetic field did not play a major role in controlling the flow. In the presence of a cylinder at a cavity angle of 0°, a vortex was formed in the absence of a magnetic field due to the moving wall of the cavity. However, the cylinder also caused irregularities (disarray) in the streamlines. Upon applying a magnetic field, the downward diversion of the flow was reduced due to the existence of the cylinder. In addition, the Lorentz force drove the flow towards the right side of the cavity. This flow diversion was more pronounced on the cylinder surface near the moving wall. In general (i.e., regardless of the existence of a magnetic field), the flow function was minimized at 90°. In the presence of a magnetic field at 90°, the streamlines were still smoother after the cylinder was placed inside the cavity; however, the vortex in the vicinity of the right cylinder in this case was the result of the flow hitting against the rotating wall.

9.7. Isotherm contours in the presence and absence of cavity cylinder

Fig. 10 shows the isotherm streamline contours obtained at two different angles in the presence and absence of a magnetic field. In the absence of a cylinder and a magnetic field at cavity angles of 0° and 90°, heat distribution inside the cavity was almost irregular, which was unlike the case where a magnetic field was applied. As exhibited by the

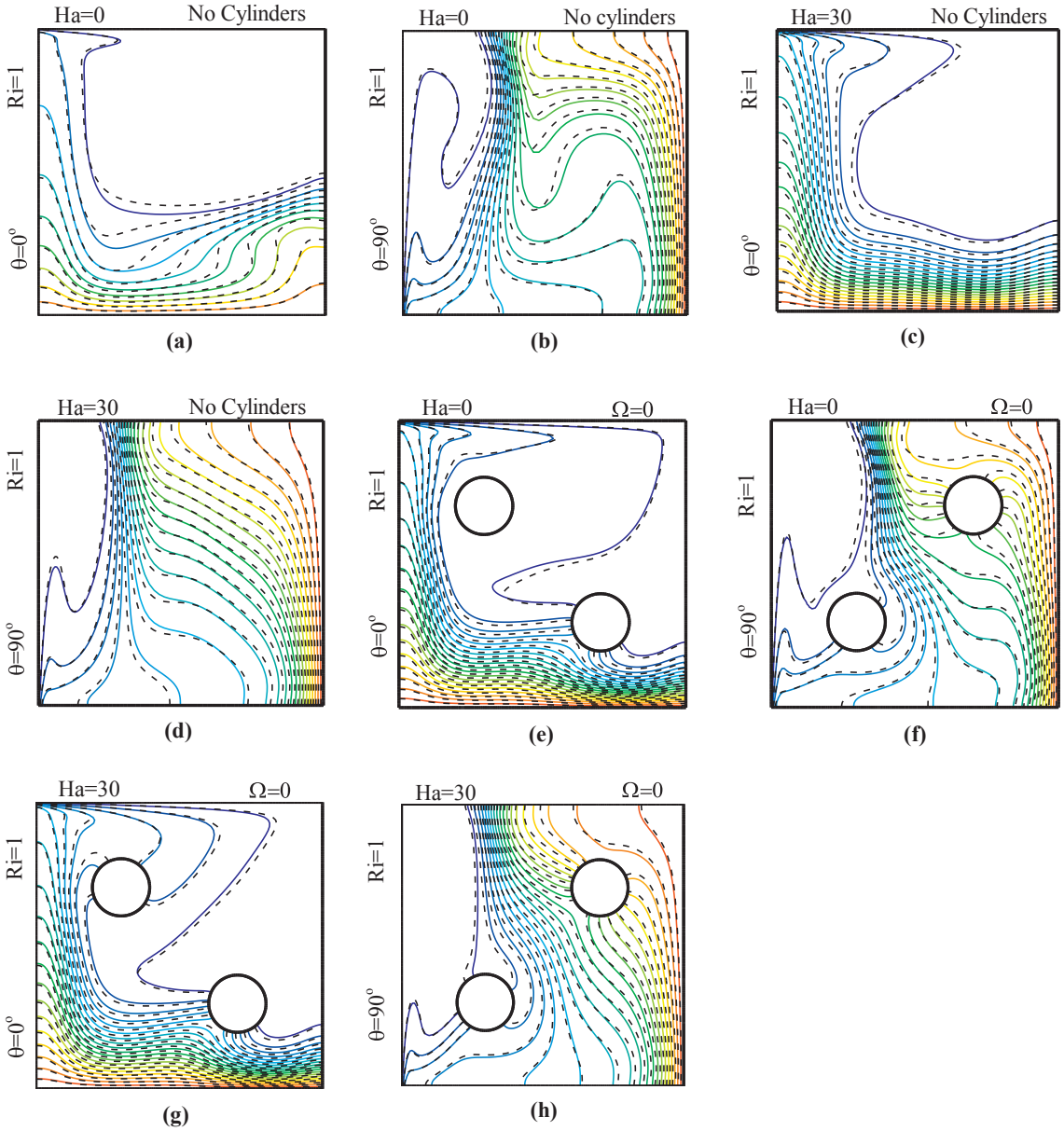

Fig. 10. Isotherm line contours in the presence and absence of cylinder, obtained at minimum and maximum Ha for two different angles.

isothermal streamlines, heat transfer in the cavity improved after applying the magnetic field. It was, therefore, expected that the presence of the magnetic field would increase the rate of heat transfer in this case. Although this result contradicted the previous results, it was concluded that the cylinder played an essential role in predicting heat transfer behavior; and, therefore, should be duly considered in the design of the system. On the other hand, in the absence of a magnetic field, the difference between the isothermal streamlines of the nanofluid and the pure fluid was influenced by the coefficient of thermal conduction. In the presence of a magnetic field, the thermal difference between these streamlines was reduced due to the reduction in the fluid velocity. At 90° in the presence of a magnetic field, uniform isothermal streamlines were observed. In addition, heat penetration into the cavity was reduced under these conditions. Similar results were obtained in the presence of a cylinder. It should be emphasized that the mere existence of the cylinder inside the cavity (even a static cylinder) would improve heat transfer and increase the relevant thermal gradients. In addition, at a cavity angle of 0°, heat penetration into the cavity was improved in the presence of a magnetic field. As the cavity angle increased to 90°, however, the opposite occurred. As can be observed, heat distribution improved in the absence of a magnetic field. Therefore, the general conclusion would be that all the cases already encountered in the present section can be regarded as exceptions.

9.8. Streamline contours for isothermal cylinders

Fig. 11 shows the streamline contours obtained for two different angles at different Richardson numbers in the following cases: (1) thermally isolated cylinders, and (2) isothermal cylinders. At constant Ri, the flow patterns obtained for thermally isolated and isothermal cylinders were, in general, not significantly different. However, a more pronounced difference was observed as Ri was increased. On the other hand, it was observed that the isothermal cylinders would either generate vortices or increase the strength of the existing ones, particularly at greater Richardson numbers. The flow function value obtained for isothermal cylinders was independent of Ri; i.e., at times more and at times less than that obtained for thermally isolated cylinders. Though no reasonable explanation was found for this, the following relationship

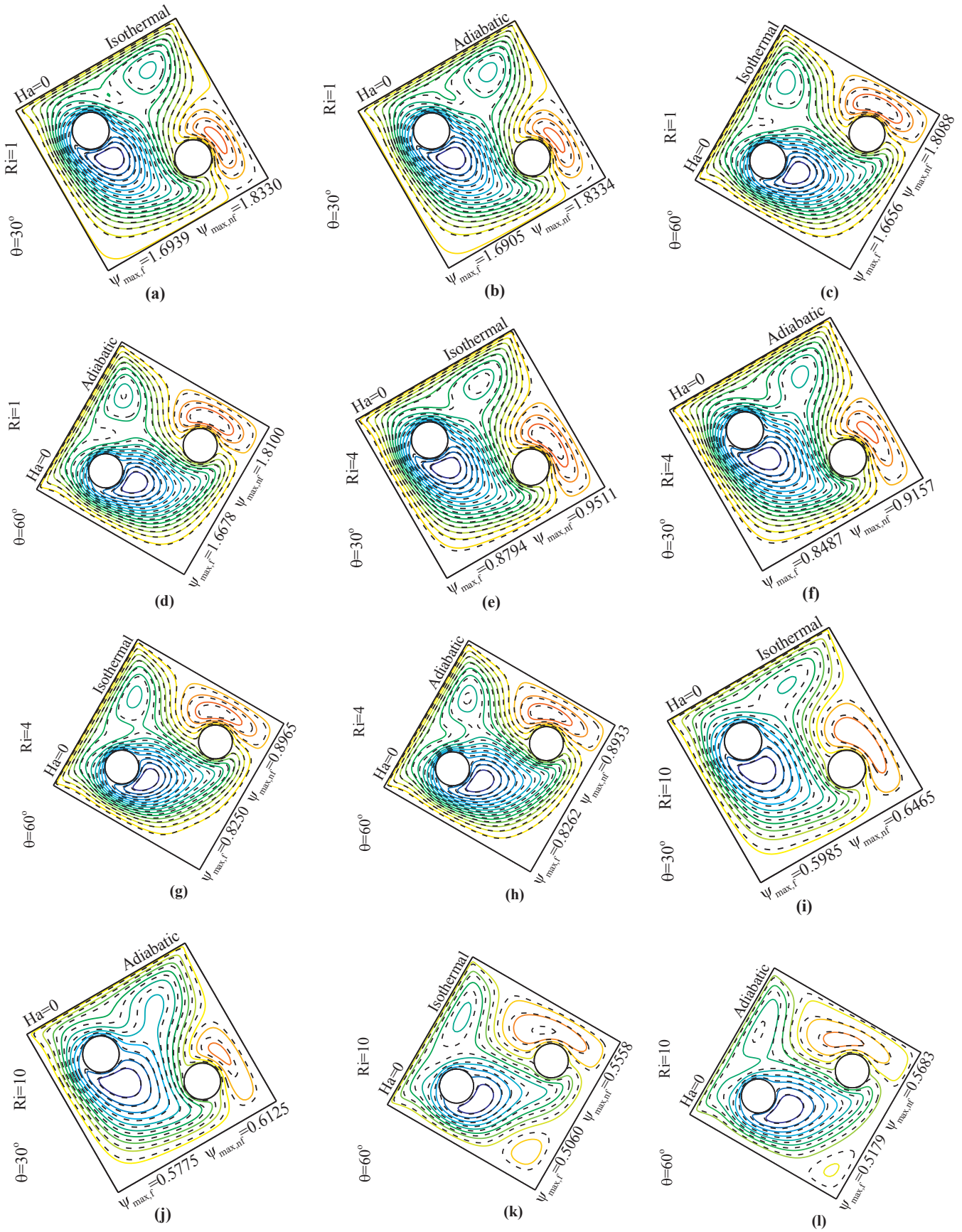

Fig. 11. Streamline contours obtained at two different angles for thermally isolated and isothermal cylinders.

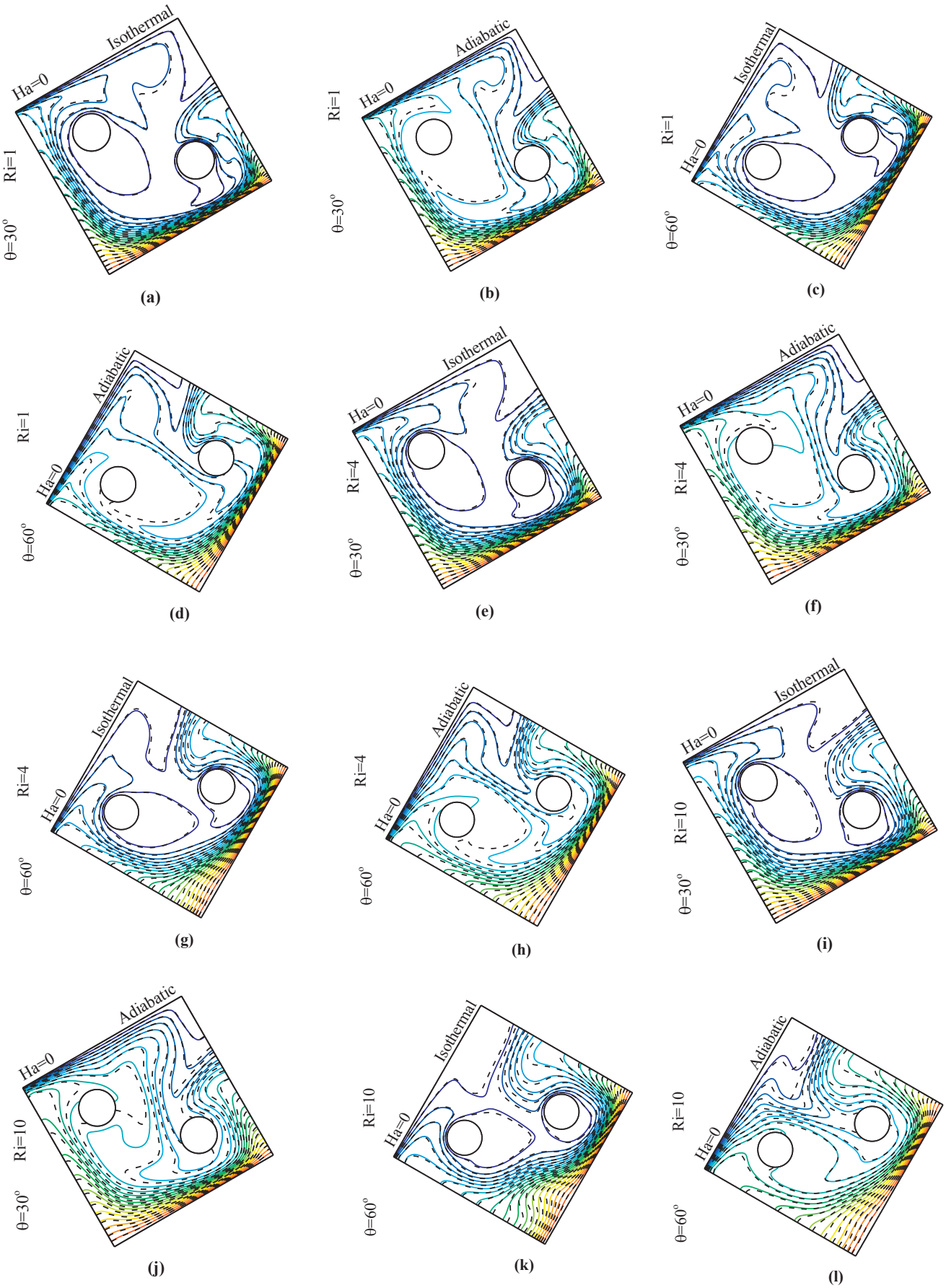

Fig. 12. Isotherm contours obtained at two different cavity angles for isothermal cylinders and thermally isolated cylinders.

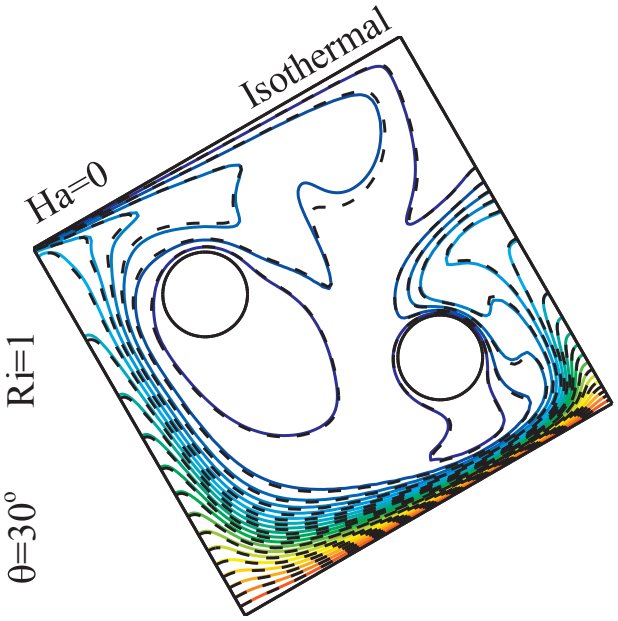

(a)

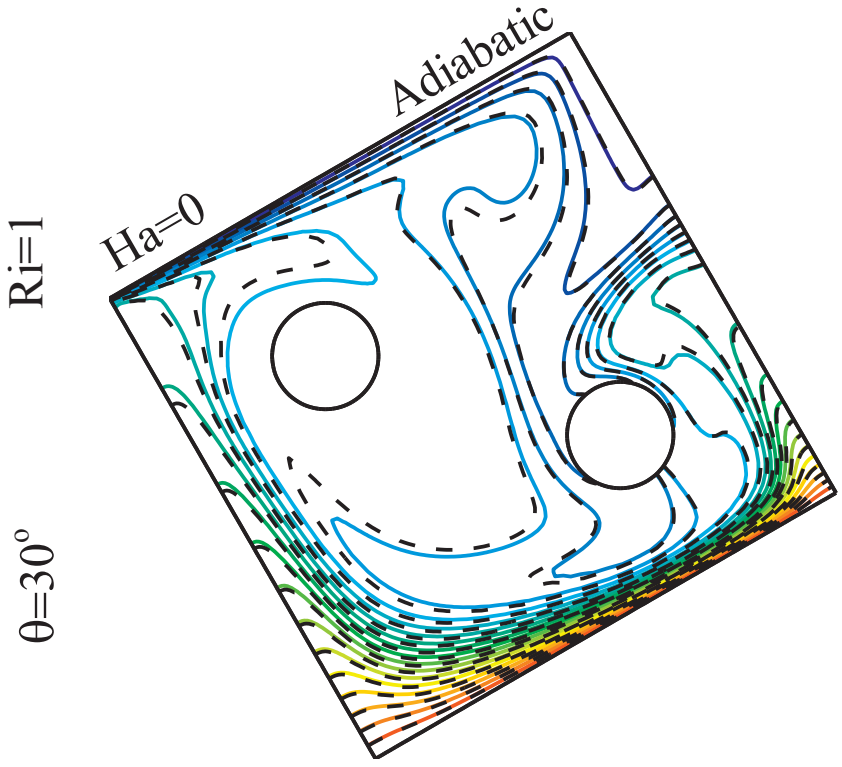

(b)

Fig. 12. (*continued*)

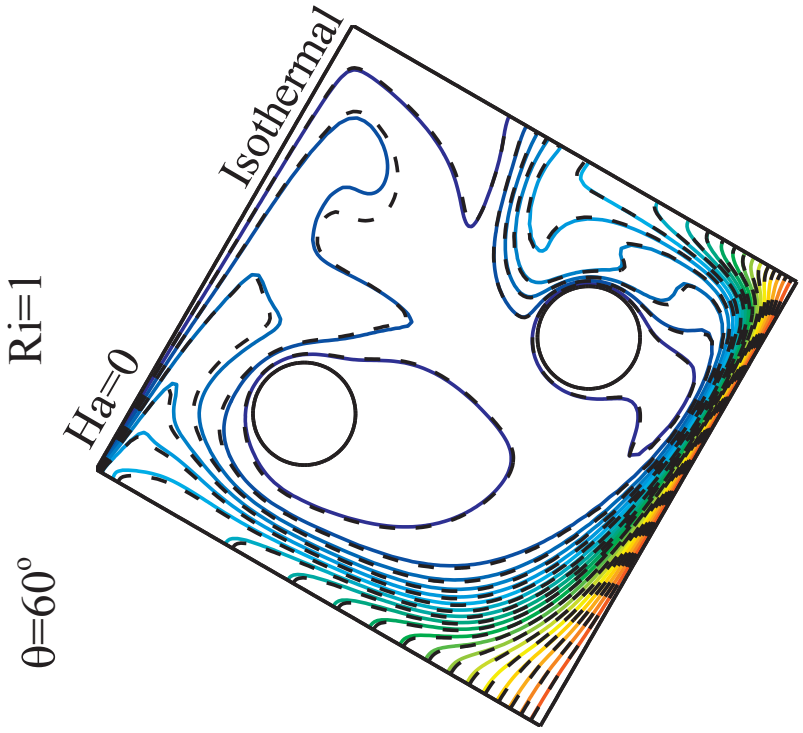

(c)

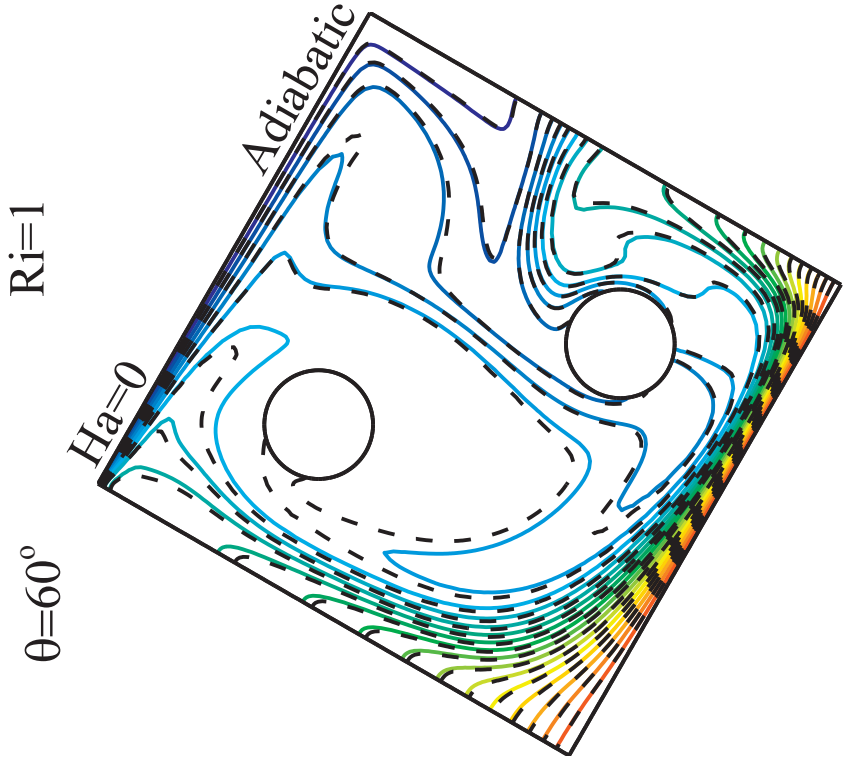

(d)

Fig. 12. (*continued*)

can be argued to exist in the case of a pure fluid: At a cavity angle of circa 30°, the flow function value obtained for the isothermal cylinders exceeded that calculated for the thermally isolated cylinders; whereas the opposite is true for the cavity angles in the vicinity of 60°.

9.9. Isotherm contours for isothermal cylinders

Fig. 12 shows the isotherm line contours obtained at two different angles and different Richardson numbers for the thermally isolated and isothermal cylinders. As can be observed, different isothermal streamline patterns resulted from these two cases. In the case of isothermal cylinders, more or less uniform (even) temperatures were obtained at the cavity center as well as at the upstream of the cylinders regardless of the Ri values. In fact, isothermality of the cylinders caused a fluid velocity increase in the region between the hot wall and the cold cylinder, thus leading to further increases in the thermal gradients which were expected to trigger a corresponding increase in the heat transfer rate. Due to the strong effect exerted by the isothermal cylinders on the isothermal streamline patterns, cold temperatures were retained in more than half the cavity, thus leading to a homogeneous temperature distribution within the cavity. Upon increasing Ri, an increase was observed in the effect of cavity angle on isothermal streamline pattern in the case where the cylinders were not thermally isolated. For example, at Ri = 10, increasing cavity angle from 30 to 60° led to distribution of heat and the subsequent reduction of heat transfer rate in this region. In addition, increasing Ri at a constant cavity angle (which reduced the rate of heat transfer) reduced the velocity and thermal gradients, and, ultimately, the rate of heat transfer.

9.10. Effect of rotational velocity of cylinders on streamline contours

Fig. 13 shows the streamline contours obtained for two different cavity angles as well as rotational velocities of the cylinder in the presence and absence of a magnetic field. As can be observed, increasing the rotational velocity accelerated fluid convection inside the cavity at both cavity angles; so much so that the flow function value was also increased. At a cavity angle of 0° in the absence of a magnetic field, increasing the rotational velocity gave rise to vortices. As can be observed, the flow at the downstream of the left cylinder was driven in opposite directions due to the increased rotational velocity. In addition, both the cylinders further strengthened the vortex that had been formed due to the motion of the wall. Similar results were obtained in the presence of a magnetic field, except for the fact that the flow rate increase was less in this case than that obtained in the absence of a magnetic field due to the action of the Lorentz force. On the other hand, the Lorentz force drove the fluid flow slightly towards the right side of the cavity. In the vicinity of the right cylinder, the convection flow fully dominated the already diminishing Lorentz force effects. Similar results were observed at a cavity angle of 90° in the absence of a magnetic field. However, it should be emphasized that, at 90°, the obtained flow function value was less than that calculated at 0° due to the reduced forced convection. At $\Omega = -2$, the vortex generated via the cavity wall motion was strengthened due to the cylinder rotation. Increasing rotational velocity of the cylinders caused the diminishing of the vortex generated by the moving wall; so that at $\Omega = -3$, the flow generated by cylinder rotation grew so strong that it completely overcame that generated by the moving wall. At a cavity angle of 90° in the presence of a magnetic field, a slightly different flow pattern was observed. The magnetic field virtually caused a strong interaction between the Lorentz and the convection forces, which resulted in the appearance of vortices at the downstream of the right cylinder as well as on the right side of the left cylinder. At constant Ha, increasing cylinder rotational velocity led to elongation or merging of these vortices.

9.11. Effect of cylinder rotation on isotherm contours

Fig. 14 shows the isotherm line contours obtained for two different angles in the presence and absence of a magnetic field at different angular velocities of the cylinders. In all the studied cases, increasing the angular velocity led to a nonhomogeneous temperature distribution in the cavity which was also accelerated due to the increase, causing the velocity gradients on the wall to increase; and ultimately increasing the heat transfer rate. Increasing the angular velocity of the cylinder caused the fluid temperature to increase with the distance from the hot wall, resulting in a corresponding rise in the thermal flux entering the cavity, which in turn increased the rate of heat transfer. As indicated by the shape of the streamlines, the fluid temperature at the cavity increased due to the increase in the angular velocity of the cylinder. The same result was obtained in the presence of a magnetic field. At a cavity angle of 90°, increasing angular velocity of the cylinder caused the cold temperature zone to be driven towards the back of the left cylinder. This in turn gave rise to convection heat transfer and, ultimately, increased the overall heat transfer rate. Similar results were obtained upon applying a magnetic field; however, the temperature distribution process slowed down somehow due to the presence of the Lorentz force.

9.12. Effect of cavity angle on heat transfer

Fig. 15 shows the average Nusselt number vs. cavity angle diagram, plotted at different Richardson numbers and volumetric fractions. As can be observed, the greatest heat transfer rate at each cavity angle occurs at a volumetric fraction of 3%. The reason for this can be the maximization of the coefficient of thermal expansion of the nanofluid at this volumetric fraction. Increasing cavity angle decreased the rate of heat transfer. As was indicated in the relation obtained for isothermal streamline contours, increasing cavity angle would lead to distribution of heat within the enclosure, thus reducing the thermal gradients in the vicinity of the hot wall, which would in turn reduce the overall thermal flux. In addition, as shown in the figure, decreasing the Richardson number increased the heat transfer rate. This was due to the fact that, upon decreasing Ri. The kinetic energy of the fluid inside the cavity would decrease, thus raising the thermal gradients and ultimately the rate of heat transfer. Moreover, at lower Richardson numbers, the heat transfer rate variation with cavity angle declined. Due to forced convection being the dominant heat transfer regime at lower Richardson numbers, the influence of cavity angle on fluid circulation within the cavity was reduced as the fluid momentum increased and the buoyancy forces became dominant. This in turn decelerated the Nusselt number variations. Increasing Ri to 100 gave rise to free convection, turning it into the dominant heat transfer regime; and accelerated the Nusselt number variation. Accordingly, at Ri = 100, Nusselt number variation was maximized due to the essential role of the buoyance force in fluid circulation. Between cavity angles of 30 and 60°, Nusselt number variation was slight due to uniform heat distribution and the existence of surface thermal gradients. Therefore, minimum heat transfer variation was expected under these circumstances. At a volumetric fraction of 1% and cavity angle of 0°, the rate of heat transfer increased by 97.36% at Ri = 1 as compared with that at Ri = 100. Similarly, the heat transfer rate increases obtained at the same cavity angle at volumetric fractions of 2% and 3% were 97.85% and 98.39%, respectively. Therefore, at Ri = 1 and cavity angel = 0°, the increase in the rate of heat transfer obtained at a volumetric fraction of 3% was 1.49% and 3% greater than the heat transfer rates obtained at volumetric fractions of 2% and 1% respectively.

9.13. Effect of Hartman number on heat transfer

Fig. 16 shows the average Nusselt number vs. Ha diagram, plotted at different volumetric fractions and cavity angles. According to this diagram, an increase in the nanofluid volumetric fraction (due to a

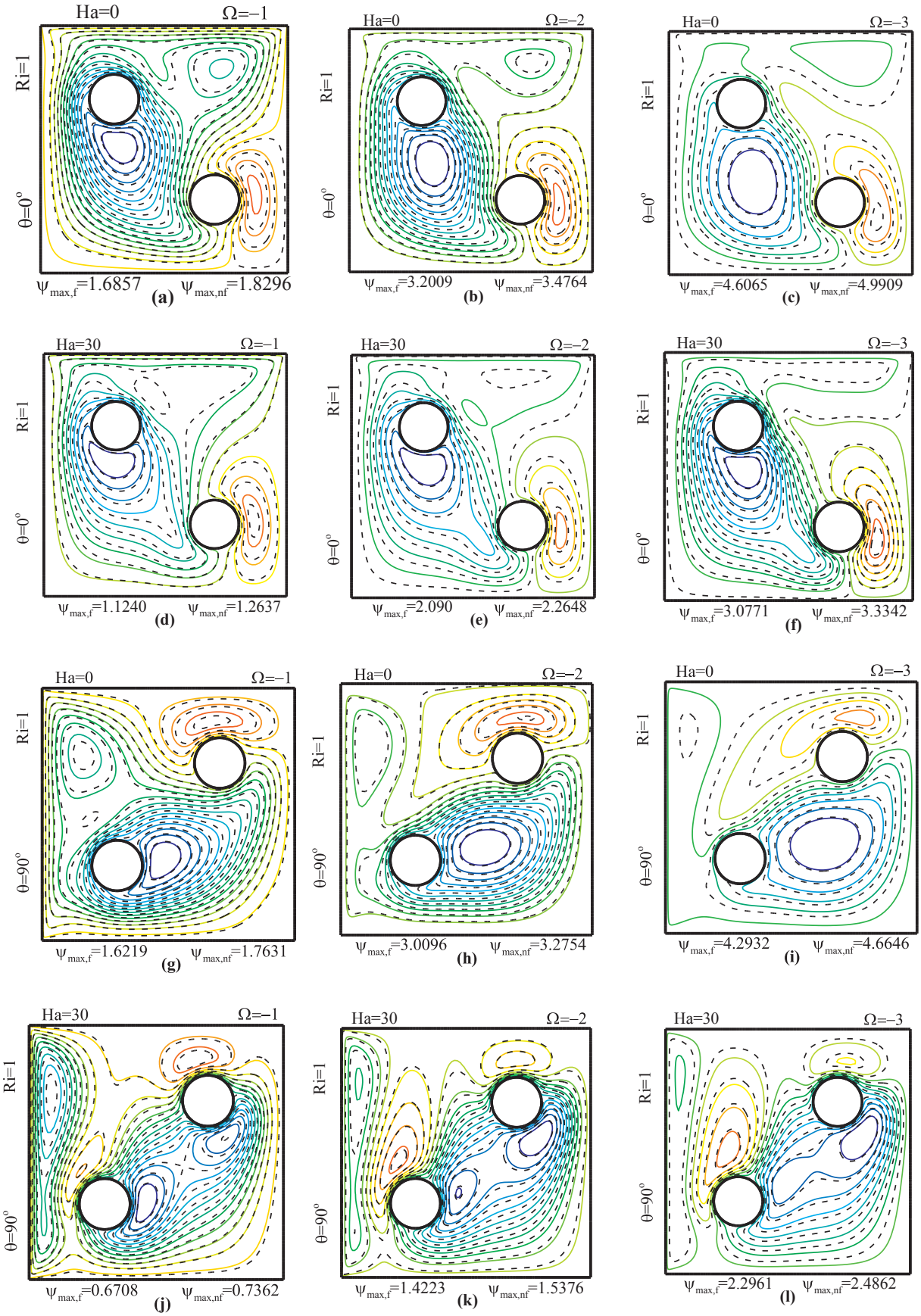

Fig. 13. Streamline contours obtained for two different angles in the presence and absence of a magnetic field at different angular velocities of cylinders.

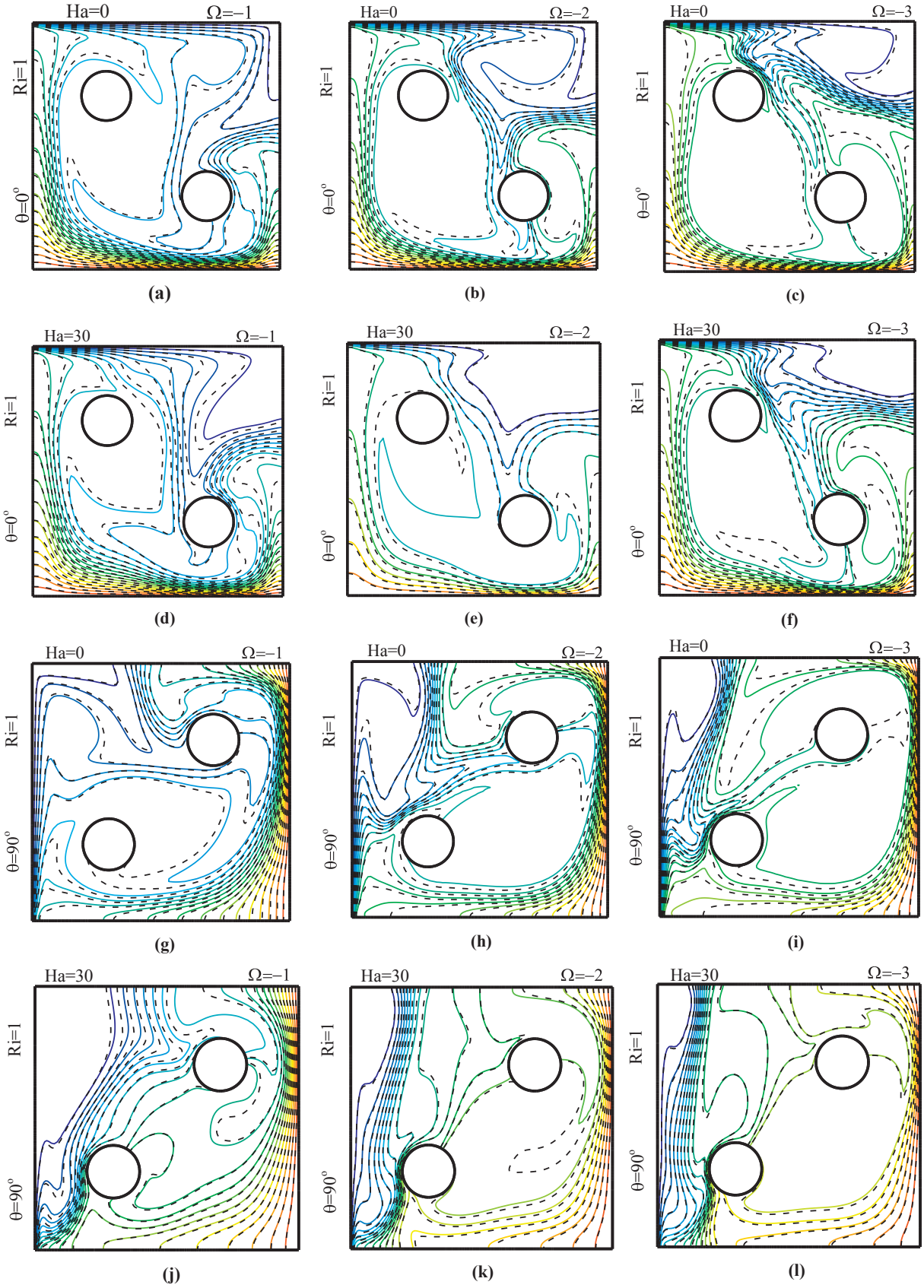

Fig. 14. Isotherm line contours obtained for two different cavity angles in the presence and absence of a magnetic field at different angular velocities of the cylinder.

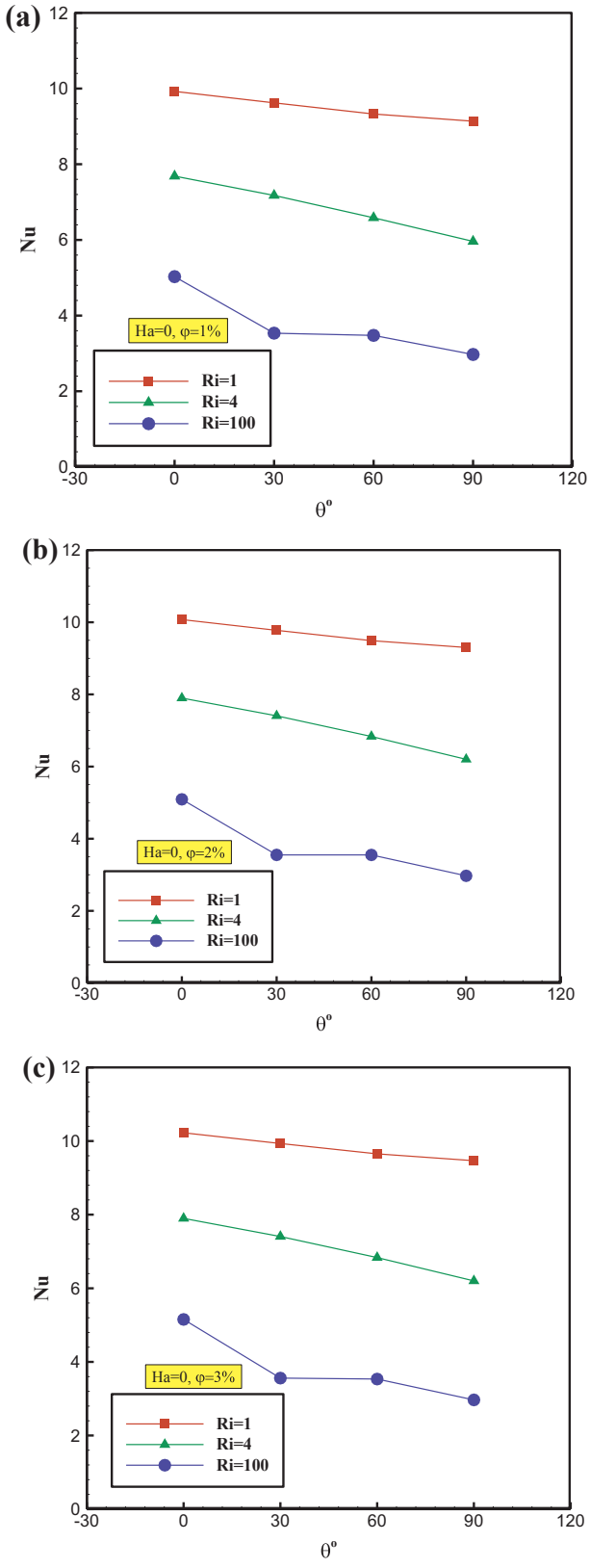

Fig. 15. Average Nusselt number vs. cavity angle at different Richardson numbers and volume fractions.

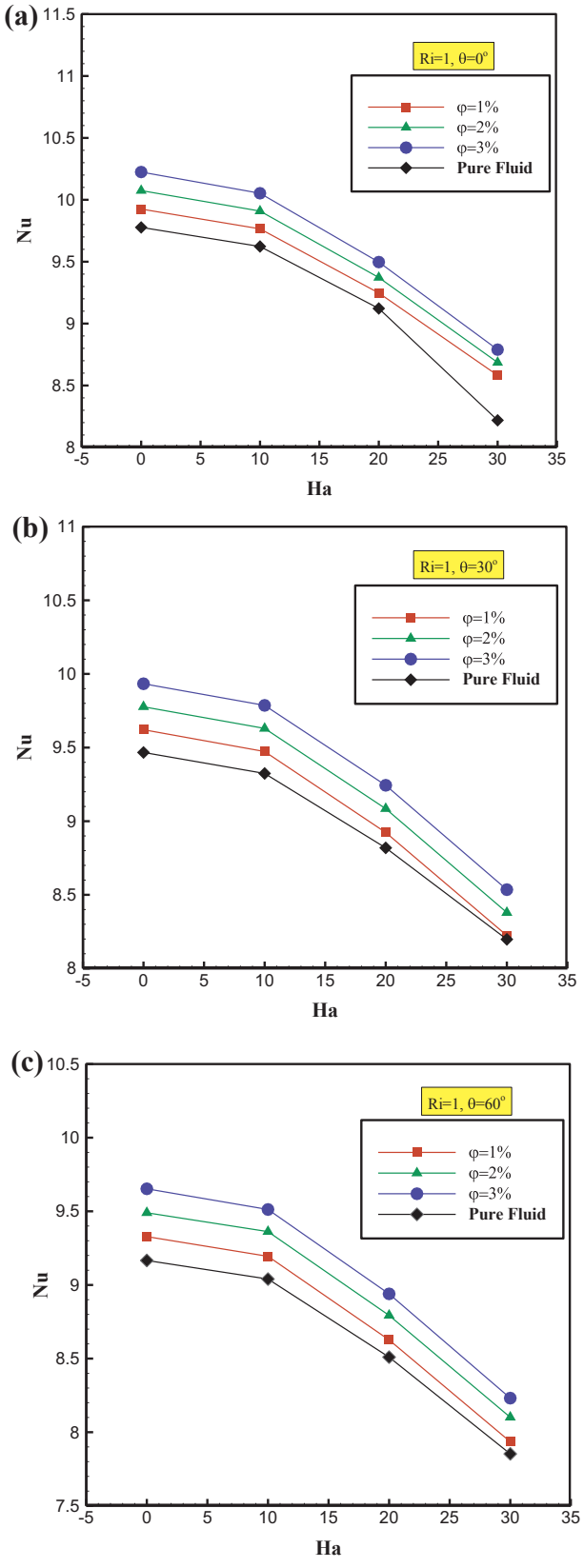

Fig. 16. Average Nusselt number vs. Ha diagram, plotted at different volumetric fractions and cavity angles.

corresponding increase in its coefficient of thermal expansion) would maximize the heat transfer rate at each cavity angle. This is a similar trend to that obtained in the previous case. Increasing Ha led to a decrease in the rate of heat transfer. As the magnetic field intensity was increased, the convection flow component of the fluid (generated due to the action of the Lorentz force) as well as the thermal gradients at the hot wall was reduced. Hence, increasing Ha gave rise to conduction

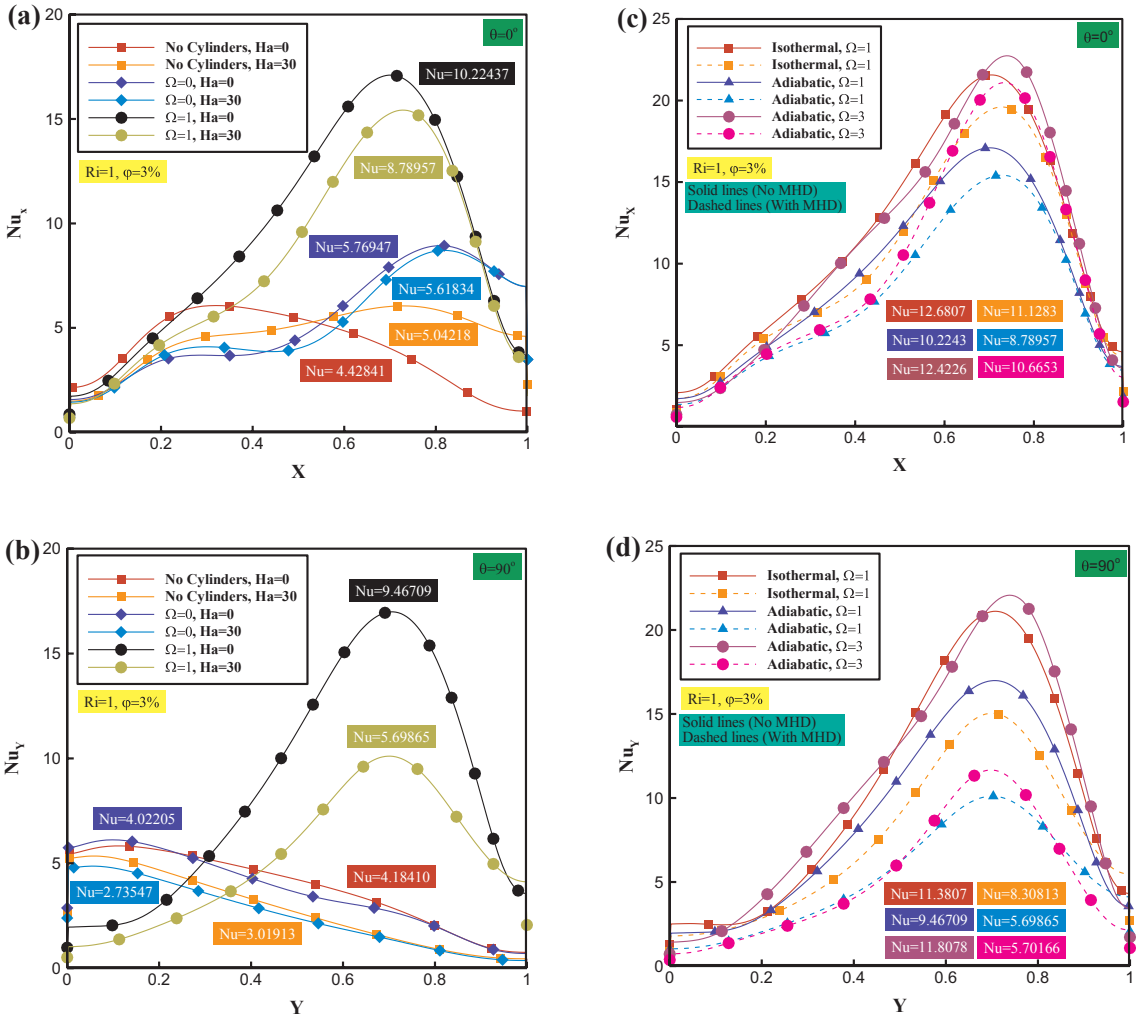

Fig. 17. Local Nusselt number vs. dimensionless cavity length characteristic, plotted at different angular velocities of the cylinder for the following cases: In the presence of a cylinder and In the absence of a cylinder (a, b); Isothermal cylinders and thermally isolated cylinders (c, d).

heat transfer within the cavity, thus effectively inhibiting the convection flows. Nusselt number variations with magnetic field intensity, demonstrated in these diagrams, were almost identical due to the dominance of the forced convection over the free convection regime. As was explained in Fig. 15, even in the absence of a magnetic field, minimum Nusselt number variation with cavity angle was observed at lower Richardson numbers. At all cavity angles, increasing Ha beyond 10 resulted in a dramatic reduction in the Nusselt number. Therefore, it can be concluded that increasing Ha from 10 to 30 would lead to the convection flow inside the cavity to be suddenly overcome by the Lorentz force in the presence of a magnetic field. At a cavity angle of 0° and a volumetric fraction of 3%, the heat transfer rates obtained in the absence of a magnetic field and at Ha = 30 were 4.57% and 6.94% greater than those obtained for a pure fluid respectively. Similarly, the heat transfer rates obtained at a volumetric fraction of 3% in the absence of a magnetic field and at Ha = 30 were 4.92% and 4.12% greater than those obtained for a pure fluid respectively. At a cavity angle of 60° and a volumetric fraction of 3%, the heat transfer rates obtained in the absence of a magnetic field and at Ha = 30 were 5.31% and 4.81% greater than those obtained for a pure fluid respectively.

9.14. Local Nusselt number variations caused by: Absence of cylinder, angular velocity of cylinder, thermal isolation of cylinder, and isothermal cylinders

Fig. 17 shows the local Nusselt number vs. dimensionless cavity length characteristic, plotted at two different cavity angles in the presence and absence of a magnetic field for the following cases: in the presence of a cylinder and in the absence of a cylinder (a,b); Isothermal cylinders and thermally isolated cylinders (c,d). In Fig. 17a, where there is no cylinder in the cavity (i.e., solid cavity walls), maximum heat transfer rate was obtained in the presence of a magnetic field. In the absence of a cylinder, the thermal gradients actually increased due to the presence of the magnetic field. In other words, presence of a cylinder inside the cavity can play a significant role in predicting the flow pattern as well as the heat transfer rate. The velocity gradients in the vicinity of the wall increased in this case due to the presence of the magnetic field. Accordingly, it was concluded that absence of the cylinder was the major cause of the conduction heat transfer being reduced. Thus, the shear stress in the y direction increased in the presence of a magnetic field. In addition, the coefficient of friction between the fluid and the wall increased due to the interaction convection flow and the Lorentz force, leading to a further increase in the rate of heat transfer. The heat transfer rate obtained in the presence of a magnetic field was 13.86% greater than that obtained in the absence of the field. The same went for a cavity angel of 90° (Fig. 17b) where the increase in

the rate of heat transfer was 38.58%. The greatest heat transfer rate was observed in the presence of a cylinder (whether static or rotating) inside the cavity. The same conditions persisted even after a DC field was applied. However, in this case, the opposite of the above occurred, namely, the magnetic field was regarded as a negative factor which inhibited heat transfer. As already mentioned, in the absence of a magnetic field, the fluid would move faster within the cavity, thus increasing the velocity divergence which would consequently increase the thermal gradient in the y direction, and ultimately, increase the rate of heat transfer. Since the flow and heat transfer patterns grew non-homogeneous due to the presence of the cylinder, the cylinder would trigger an increase in the convection heat transfer flow which would, in turn, increase the overall heat transfer rate, thus maximizing heat transfer rate when the cylinder was rotating. In addition, it was observed that the greatest Nusselt number was obtained at $\Omega = -1$ in the X and Y intervals of [0.703 0.726] and [0.691 0.708] at cavity angles of 0° and 90° respectively. This was due to the fact that rotation of the right cylinder increased the convection heat transfer coefficient due to this cylinder being in the proximity of the hot cavity wall. Similar results were obtained for $\Omega = 0$ at a cavity angle of 0°. At a cavity angle of 90°, however, the flow pattern underwent a change due to the interaction between the gravity and the buoyancy forces as well as the position of the right cylinder. As a result of this change, the flow was pulled (diverted) downwards, thus maximizing the fluid velocity at the downstream of the right cylinder, and ultimately, maximizing the local Nusselt number in the $0.052 \le Y \le 0.098$ interval. As observed in Fig. 17c and 17d, the increase in the angular velocity of the cylinder (due to the increased convection flow inside the cylinder) led to a corresponding increase in the rate of heat transfer, with the maximum rate occurring at $\Omega = -3$ and a cavity angle of 0°. On the other hand, the heat transfer rate was greatly influenced due to the cylinders being isothermal (T = Tc). At an identical angular velocity of $\Omega = -1$, the rate of heat transfer obtained for isothermal cylinders was far greater than that obtained for thermally isolated cylinders. In fact, in the case of isothermal cylinders, the heat exchange distance was reduced (due to the cylinders being at the same temperature), causing an increase in the fluid velocity in the region between the cylinders and the cavity wall, which ultimately led to a significant raise in the rate of heat transfer. At a cavity angle of 0°, the effect of isothermal cylinders at $\Omega = -1$ was far greater than that exhibited by the thermally isolated cylinders at $\Omega = -3$. The rate of heat transfer in the presence and absence of a magnetic field for isothermal cylinders at $\Omega = -1$ were 26.6% and 24% greater than those obtained for the thermally isolated cylinders. Similar results were obtained at a cavity angle of 90°. However, a more conclusive statement would be "To achieve maximum heat transfer rate, the angular velocity of the cylinder must be greater than -3 ($\Omega > -3$)." Further increase of the rotational velocity led to a less uniform diagram.

9.15. Effect of Ha number on entropy generation

Fig. 18 shows the dimensionless total entropy generation vs. Ha diagrams, plotted at different Richardson numbers and cavity angles. In all the studied cases, the minimum and maximum entropy generations were obtained at Ri = 100 and Ri = 1, respectively. According to the total entropy generation formula, as entropy generation in each section is directly proportional to the gradients of that section, and as the gradients are maximized at Ri = 1, entropy generation would also occur at Ri = 1. Increasing Ha led to a decrease in entropy generation due to the decline of the velocity and thermal gradients in the presence of the magnetic field. It should be emphasized that heat transfer and viscous effects play the most and the least important parts in entropy generation respectively. On the other hand, entropy generation due to viscous effects increased with Ri. However, this increase could not overcome the entropy generation resulting from heat transfer effects. As already mentioned in the section on streamlines and isothermal

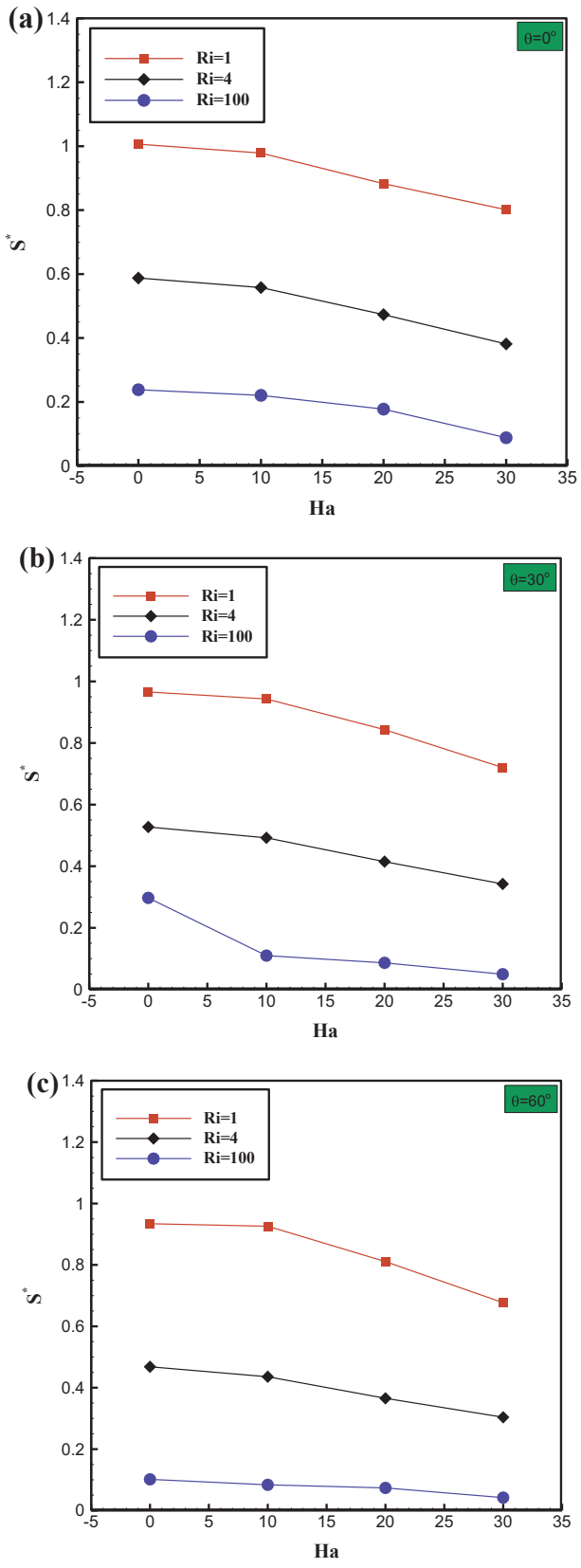

Fig. 18. Dimensionless total entropy generation vs. Ha number at different Richardson numbers and cavity angles.

contours, increasing cavity angle would the slope angle to influence the gradients by causing them to decrease with this angle. Variation as well as slope of the diagram at Ri = 1 and Ri = 4 were similar at all the three angles. However, at Ri = 100, the conditions were different. At constant buoyancy force, the diminishing forced convection flow replaced by a dominant natural convection regime in the cavity. Presence of a large volumetric force in the cavity made the new force highly dependent on the slope angle, ultimately resulting in an uneven behavior in terms of total entropy generation.

10. Conclusion

In this paper, MHD mixed convection and entropy generation in a cavity containing nanofluid with two rotating cylinders was carried out. In this study, a two-phase approach (mixture model) was used to simulate flow and heat transfer. The results of this study are as follows:

- Increasing the Hartmann number leads to a reduction in heat transfer. But increasing the Hartman number can play an effective role in controlling the fluid flow.
- The increase in heat transfer rate in isothermal cylinders is higher than insulating cylinders.
- The presence of the cylinder inside the cavity has a significant role in improving the heat transfer.
- As the angular velocity of the cylinder increases, heat transfer is improved.
- As the Hartman number decreases, the amount of total entropy generation increases.
- The highest heat transfer rate occurs at a cavity angle of 0° for a volume fraction of 3%.

References

[1] M.M. Rashidi, S. Abelman, N. Freidooni Mehr, Entropy generation in steady MHD flow due to a rotating porous disk in a nanofluid, Int. J. Heat Mass Transf. 62 (2013) 515–525.
[2] Amir Houshang Mahmoudi, Ioan Pop, Mina Shahi, Farhad Talebi, MHD natural convection and entropy generation in a trapezoidal enclosure using Cu–water nanofluid, Comput. Fluids 72 (2013) 46–62.
[3] M. Sheikholeslami, M. Gorji-Bandpy, D.D. Ganjim, Numerical investigation of MHD effects on Al2O3-water nanofluid flow and heat transfer in a semi-annulus enclosure using LBM, Energy 60 (2013) 501–510.
[4] Cha'o-Kuang Chen, Bo-Shiuan Chen, Chin-Chia Liu, Entropy generation in mixed convection magnetohydrodynamic nanofluid flow in vertical channel, Int. J. Heat Mass Transf. 91 (2015) 1026–1033.
[5] A. Malvandi, M.R. Safaei, M.H. Kaffash, D.D. Ganji, MHD mixed convection in a vertical annulus filled with Al2O3–water nanofluid considering nanoparticle migration, J. Magn. Magn. Mater. 382 (2015) 296–306.
[6] I. Fersadoua, H. Kahalerras, M. El Ganaoui, MHD mixed convection and entropy generation of a nanofluid in a vertical porous channel, Comput. Fluids 121 (2015) 164–179.
[7] Zouhaier Mehrez, Afif El Cafsi, Ali Belghith, Patrick Le Quéré, MHD effects on heat transfer and entropy generation of nanofluid flow in an open cavity, J. Magn. Magn. Mater. 374 (2015) 214–224.
[8] Fatih Selimefendigil, Hakan F. Öztop, Influence of inclination angle of magnetic field on mixed convection of nanofluid flow over a backward facing step and entropy generation, Adv. Powder Technol. 26 (2015) 1663–1675.
[9] N. Hajialigol, A. Fattahi, M. Haji Ahmadi, M. Ebrahim Qomi, E. Kakoli, MHD mixed convection and entropy generation in a 3D microchannel using Al2O3–water nanofluid, J. Taiwan Inst. Chem. Eng. 46 (2015) 30–42.
[10] M. Sheikholeslami, T. Hayat, A. Alsaedi, MHD free convection of Al2O3–water nanofluid considering thermal radiation: a numerical study, Int. J. Heat Mass Transf. 96 (2016) 513–524.
[11] Fatih Selimefendigil, Hakan F. Öztop, MHD mixed convection and entropy generation of power law fluids in a cavity with a partial heater under the effect of a rotating cylinder, Int. J. Heat Mass Transf. 98 (2016) 40–51.
[12] G.H.R. Kefayati, Simulation of heat transfer and entropy generation of MHD natural convection of non-Newtonian nanofluid in an enclosure, Int. J. Heat Mass Transf. 92 (2016) 1066–1089.
[13] M. Mamourian, K. Milani Shirvan, R. Ellahi, A.B. Rahimi, Optimization of mixed convection heat transfer with entropy generation in a wavy surface square lid-driven cavity by means of Taguchi approach, Int. J. Heat Mass Transf. 102 (2016) 544–554.
[14] S. Hussain, K. Mehmood, M. Sagheer, MHD mixed convection and entropy generation of water–alumina nanofluid flow in a double lid driven cavity with discrete heating, J. Magn. Magn. Mater. 419 (2016) 140–155.
[15] P. Barnoon, D. Toghraie, F. Eslami, B. Mehmandoust, Entropy generation analysis of different nanofluid flows in the space between two concentric horizontal pipes in the presence of magnetic field: Single-phase and two-phase approaches, Comput. Math. Appl. 77 (2019) 662–692.
[16] M. Manninen, V. Taivassalo, S. Kallio, On the mixture model for multiphase flow, Tech. Res. Centre Finland (1996).
[17] L. Schiller, A. Naumann, A drag coefficient correlation, Vdi Zeitung 77 (1935) 51.
[18] J.C. Maxwell, Treatise on Electricity and Magnetism, Clarendon Press, Oxford, 1873.
[19] H. Brinkman, The viscosity of concentrated suspensions and solutions, J. Chem. Phys. 20 (1952) 571–577.
[20] B.C. Pak, Y.1. Cho, Hydrodynamic and heat transfer study of dispersed fluids with submicron metallic oxide particles, Exp. Heat Transfer Int. J. 11 (2) (1998) 141–170.
[21] Y. Xuan, W. Roetzel, Conceptions for heat transfer correlation of nanofluids, Int. J. Heat Mass Transfer 43 (19) (2000) 3701–3707.
[22] M. Victor, R. Sreedhara, Mixed convection nanofluid flows in the presence of an applied magnetic field, Int. J. Heat Mass Transf. 107 (2017) 133–145.
[23] K. Khanafer, S.M. Aithal, Laminar mixed convection flow and heat transfer characteristics in a lid driven cavity with a circular cylinder, Int. J. Heat Mass Transf. 66 (2013) 200–209.
[24] B. Ghasemi, S.M. Aminossadati, A. Raisi, Magnetic field effect on natural convection in a nanofluid-filled square enclosure, Int. J. Therm. Sci. 50 (2011) 1748–1756.
[25] P. Barnoon, D. Toghraie, Numerical investigation of laminar flow and heat transfer of non-Newtonian nanofluid within a porous medium, Powder Technol. 325 (2018) 78–91.
[26] A. Bejan, Second law analysis in heat transfer, Energy 5 (1980) 720–732.
[27] A. Albojamal, K. Vafai, Analysis of single phase, discrete and mixture models, in predicting nanofluid transport, Int. J. Heat Mass Transf. 114 (2017) 225–237.
[28] F. Selimefendigil, H. Oztop, Modeling and optimization of MHD mixed convection in a lid-driven trapezoidal cavity Þlled with alumina-water nanoßuid: effects of electrical conductivity models, Int. J. Mech. Sci. (2017), https://doi.org/10.1016/j.ijmecsci.2017.12.035.
[29] C.J. Ho, W.K. Liu, C.C. Lin, Natural convection heat transfer of alumina-water nanofluid invertical square enclosures: an experimental study, Int. J. Therm. Sci. 49 (2010) 1345–1353.
[30] S.Y. Motlagh, H. Soltanipour, Natural convection of Al2O3-water nanofluid in an inclined cavity using Buongiorno's two-phase model, Int. J. Therm. Sci. 111 (2017) 310–320.
[31] S. Nadeem, Shafiq Ahmad, Noor Muhammad, Computational study of Falkner-Skan problem for a static and moving wedge, Sens. Actuators, B (2018) 263.
[32] M. Rashid, Iqra Shahzadi, S. Nadeem, Corrugated walls analysis in microchannels through porous medium under Electromagnetohydrodynamic (EMHD) effects Results in Physics Volume 9, June 2018, Pages 171-182.
[33] Hina Sadaf, Muhammad Usman Akbar, S. Nadeem , Induced magnetic field analysis for the peristaltic transport of non-Newtonian nanofluid in an annulus, Mathematics and Computers in Simulation (Volume 148, June 2018, Pages 16-36.
[34] Nadeem Abbas, S. Saleem, S. Nadeem, A.A. Alderremy, A.U. Khan, On stagnation point flow of a micro polar nanofluid past a circular cylinder with velocity and thermal slip, Results in Physics 9 (2018) 1224–1232.
[35] Fiaz Ur Rehman, Sohail Nadeem, Hafeez Ur Rehman, Rizwan Ul Haq, Thermophysical analysis for three-dimensional MHD stagnation-point flow of nanomaterial influenced by an exponential stretching surface, Results Phys. 8 (2018) 316–323.
[36] Hina Sadaf, Sohail Nadeem, Analysis of combined convective and viscous dissipation effects for peristaltic flow of rabinowitsch, Fluid Model J. Bionic Eng. 14 (1) (2017) 182–190.
[37] Ashfaq Ahmed, Sohail Nadeem, Effects of magnetohydrodynamics and hybrid nanoparticles on a micropolar fluid with 6-types of stenosis, Results Phys. 7 (2017) 4130–4139.
[38] A. Arabpour, A. Karimipour, D. Toghraie, The study of heat transfer and laminar flow of kerosene/multi-walled carbon nanotubes (MWCNTs) nanofluid in the microchannel heat sink with slip boundary condition, J. Therm. Anal. Calorim. 131 (2) (2018) 1553–1566.
[39] M. Hemmat Esfe, H. Hajmohammad, D. Toghraie, H. Rostamian, O. Mahian, S. Wongwises, Multi-objective optimization of nanofluid flow in double tube heat exchangers for applications in energy systems, Energy 137 (2017) 160–171.
[40] N.N. Esfahani, D. Toghraie, M. Afrand, A new correlation for predicting the thermal conductivity of ZnO–Ag (50%–50%)/water hybrid nanofluid: An experimental study, Powder Technol. 323 (2018) 367–373.
[41] S. Morteza Mousavi, A. Ali Rabienataj Darzi, Omid ali Akbari, Davood Toghraie, Ali Marzban, Numerical study of biomagnetic fluid flow in a duct with a constriction affected by a magnetic, Field 473 (2019) 42–50.
[42] Masoud Afrand, Davood Toghraie, Arash Karimipour, Somchai Wongwises, A numerical study of natural convection in a vertical annulus filled with gallium in the presence of magnetic field, J. Magn. Magn. Mater. 430 (2017) 22–28.
[43] Shahin Foroutan, Amin Haghshenas, Mohammad Hashemian, S. Ali Eftekhari, Davood Toghraie, Spatial buckling analysis of current-carrying nanowires in the presence of a longitudinal magnetic field accounting for both surface and nonlocal effects, Physica E 97 (2018) 191–205.
[44] Ramin Sarlak, Shahrouz Yousefzadeh, Omid Ali Akbari, Davood Toghraie, Sajad Sarlak, Fattah Assadi, The investigation of simultaneous heat transfer of water/Al2O3 nanofluid in a close enclosure by applying homogeneous magnetic field, Int. J. Mech. Sci. 133 (2017) 674–688.
[45] Masoud Afrand, Davood Toghraie, Nima Sina, Experimental study on thermal

conductivity of water-based Fe3O4 nanofluid: development of a new correlation and modeled by artificial neural network, Int. Commun. Heat Mass Transfer 75 (2016) 262–269.
[46] Davood Toghraie, Seyed Mohammadbagher Alempour, Masoud Afrand, Experimental determination of viscosity of water based magnetite nanofluid for application in heating and cooling systems, J. Magn. Magn. Mater. 417 (2016) 243–248.
[47] Bijan Karbasifar, Mohammad Akbari, Davood Toghraie, Mixed convection of Water-Aluminum oxide nanofluid in an inclined lid-driven cavity containing a hot elliptical centric cylinder, Int. J. Heat Mass Transf. 116 (2018) 1237–1249.
[48] F. Pourfattah, M. Motamedian, G. Sheikhzadeh, D. Toghraie, O.A. Akbari, The numerical investigation of angle of attack of inclined rectangular rib on the turbulent heat transfer of Water-Al2O3 nanofluid in a tube, Int. J. Mech. Sci. 131 (2017) 1106–1116.
[49] R. Mashayekhi, E. Khodabandeh, M. Bahiraei, L. Bahrami, D. Toghraie, Application of a novel conical strip insert to improve the efficacy of water–Ag nanofluid for utilization in thermal systems: a two-phase simulation, Energy Convers. Manage. 151 (2017) 573–586.
[50] O. Rezaei, O.A. Akbari, A. Marzban, D. Toghraie, F. Pourfattah, R. Mashayekhi, The numerical investigation of heat transfer and pressure drop of turbulent flow in a triangular microchannel, Physica E 93 (2017) 179–189.
[51] M. Heydari, D. Toghraie, O.A. Akbari, The effect of semi-attached and offset mid-truncated ribs and Water/TiO2 nanofluid on flow and heat transfer properties in a triangular microchannel, Therm. Sci. Eng. Progress 2 (2017) 140–150.